

Maximal Spontaneous Photon Emission and Energy Loss from Free Electrons

Yi Yang^{1,*}, Aviram Massuda¹, Charles Roques-Carmes¹, Steven E. Kooi², Thomas Christensen¹, Steven G. Johnson¹, John D. Joannopoulos^{1,2}, Owen D. Miller^{3,†}, Ido Kaminer^{1,4,‡}, and Marin Soljačić¹

¹Research Laboratory of Electronics, Massachusetts Institute of Technology, Cambridge, Massachusetts 02139, USA

²Institute for Soldier Nanotechnologies, 77 Massachusetts Avenue, Cambridge, Massachusetts 02139, USA

³Department of Applied Physics & Energy Sciences Institute, Yale University, New Haven, CT 06520, USA and

⁴Andrew & Erna Viterbi Department of Electrical Engineering, Technion-Israel Institute of Technology, 32000 Haifa, Israel

Free electron radiation such as Cerenkov [1], Smith–Purcell [2], and transition radiation [3, 4] can be greatly affected by structured optical environments, as has been demonstrated in a variety of polaritonic [5, 6], photonic-crystal [7], and metamaterial [8–10] systems. However, the amount of radiation that can ultimately be extracted from free electrons near an arbitrary material structure has remained elusive. Here we derive a fundamental upper limit to the spontaneous photon emission and energy loss of free electrons, regardless of geometry, which illuminates the effects of material properties and electron velocities. We obtain experimental evidence for our theory with quantitative measurements of Smith–Purcell radiation. Our framework allows us to make two predictions. One is a new regime of radiation operation—at subwavelength separations, slower (nonrelativistic) electrons can achieve stronger radiation than fast (relativistic) electrons. The second is a divergence of the emission probability in the limit of lossless materials. We further reveal that such divergences can be approached by coupling free electrons to photonic bound states in the continuum (BICs) [11–13]. Our findings suggest that compact and efficient free-electron radiation sources from microwaves to the soft X-ray regime may be achievable without requiring ultrahigh accelerating voltages.

The Smith–Purcell effect epitomizes the potential of free-electron radiation. Consider an electron at velocity $\beta = v/c$ traversing a structure with periodicity a ; it generates far-field radiation at wavelength λ and polar angle θ , dictated by [2]

$$\lambda = \frac{a}{m} \left(\frac{1}{\beta} - \cos \theta \right), \quad (1)$$

where m is the integer diffraction order. The absence of a minimum velocity in Eq. (1) offers prospects for threshold-free and spectrally tunable light sources, spanning from microwave and Terahertz [14–16], across visible [17–19], and towards X-ray [20] frequencies. In stark contrast to the simple momentum-conservation determination of wavelength and angle, there is no unified yet simple analytical equation for the radiation *intensity*. Previous theories only offer explicit solutions either under strong assumptions (e.g., assuming perfect conductors or employing effective medium descriptions) or for simple, symmetric geometries [21–23]. Consequently, heavily numerical strategies are often an unavoidable resort [24, 25]. The inherent complexity of the interactions

between electrons and photonic media have prevented a more general understanding of how pronounced Smith–Purcell radiation and its siblings can ultimately be for *arbitrary* structures, and consequently, how to design the maximum enhancement for free-electron light-emitting devices.

We begin our analysis by considering an electron (charge $-e$) of constant velocity $v\hat{\mathbf{x}}$ traversing a generic scatterer (plasmonic or dielectric, finite or extended) of arbitrary size and material composition, as in Fig. 1(a). The free current density of the electron, $\mathbf{J}(\mathbf{r}, t) = -\hat{\mathbf{x}}ev\delta(y)\delta(z)\delta(x - vt)$, generates a frequency-dependent ($e^{-i\omega t}$ convention) incident field [27]

$$\mathbf{E}_{\text{inc}}(\mathbf{r}, \omega) = \frac{e\kappa_\rho e^{ik_v x}}{2\pi\omega\epsilon_0} [\hat{\mathbf{x}}i\kappa_\rho K_0(\kappa_\rho\rho) - \hat{\rho}k_v K_1(\kappa_\rho\rho)], \quad (2)$$

written in cylindrical coordinates (x, ρ, ψ) ; here, K_n is the modified Bessel function of the second kind [28], $k_v = \omega/v$, and $\kappa_\rho = \sqrt{k_v^2 - k^2} = k/\beta\gamma$ ($k = \omega/c$, free-space wavevector; $\gamma = 1/\sqrt{1 - \beta^2}$, Lorentz factor). Hence, the photon emission and energy loss of free electrons can be treated as a scattering problem: the electromagnetic fields $\mathbf{F}_{\text{inc}} = (\mathbf{E}_{\text{inc}}, Z_0\mathbf{H}_{\text{inc}})^T$ (for free-space impedance Z_0) are incident upon a photonic medium with material susceptibility χ (a 6×6 tensor for a general medium), causing both absorption and far-field scattering—i.e., photon emission—that together comprise electron energy loss [Fig. 1(a)].

As recently shown in Refs. [29–31], for a generic electromagnetic scattering problem, passivity—the condition that polarization currents do no net work—constrains the maximum optical response from a given incident field. Consider three power quantities derived from \mathbf{F}_{inc} and the total field \mathbf{F} within the scatterer volume V : the total power lost by the electron, $P_{\text{loss}} = -(1/2)\text{Re} \int_V \mathbf{J}^* \cdot \mathbf{E} dV = (\epsilon_0\omega/2)\text{Im} \int_V \mathbf{F}_{\text{inc}}^\dagger \chi \mathbf{F} dV$, the power absorbed by the medium, $P_{\text{abs}} = (\epsilon_0\omega/2)\text{Im} \int_V \mathbf{F}^\dagger \chi \mathbf{F} dV$, and their difference, the power radiated to the far field, $P_{\text{rad}} = P_{\text{loss}} - P_{\text{abs}}$. Treating \mathbf{F} as an independent variable, the total loss P_{loss} is a *linear* function of \mathbf{F} , whereas the fraction that is dissipated is a *quadratic* function of \mathbf{F} . Passivity requires nonnegative radiated power, represented by the inequality $P_{\text{abs}} < P_{\text{loss}}$, which in this framework is therefore a *convex* constraint on any response function. Constrained maximization (see Supplementary 1) of the energy-loss and photon-emission power quantities, P_{loss} and

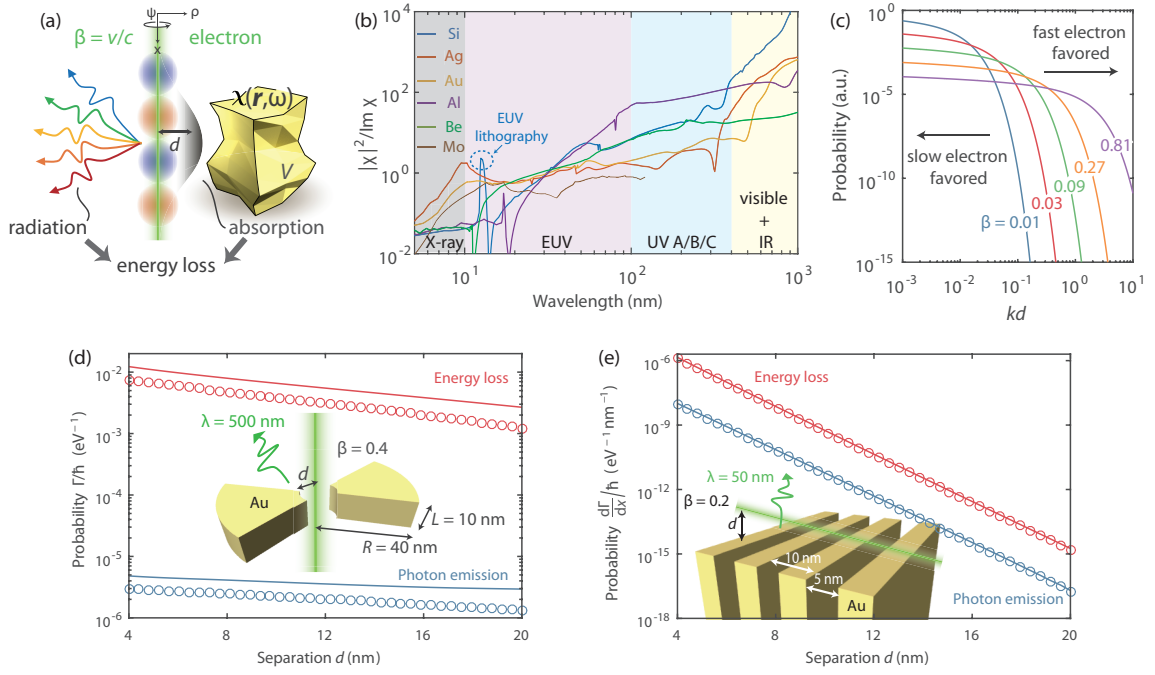


Figure 1. **Theoretical framework and predictions.** (a) The interaction between a free electron and an obstacle defined by a susceptibility tensor $\chi(\mathbf{r}, \omega)$ within a volume V , located at a distance d , generates electron energy loss into radiation and absorption. (b) $|\chi|^2/\text{Im}\chi$ constrains the maximum material response to the optical excitations of free electrons over different spectral ranges for representative materials (from Ref. [26]). At the X-ray and EUV regime, Si is optimal near the technologically relevant 13.5 nm (dashed circle). Contrary to the image charge intuition for the optical excitations of electrons, low-loss dielectrics (such as Si in the visible and infrared regimes) can be superior to metals. (c) Shape-independent upper limit showing superiority of slow or fast electrons at small or large separations; the material χ only affects the overall scaling. (d–e) Numerical simulations (circles) compared to analytical upper limits [lines; Eq. (5a) for (d) and Eq. (6) for (e), respectively] for the radiation (blue) and energy loss (red) of electrons (d) penetrating the center of an annular bowtie antenna and (e) passing above a grating.

P_{rad} , directly yields the limits

$$P_{\tau}(\omega) \leq \frac{\epsilon_0 \omega \xi_{\tau}}{2} \int_V \mathbf{F}_{\text{inc}}^{\dagger} \chi^{\dagger} (\text{Im} \chi)^{-1} \chi \mathbf{F}_{\text{inc}} dV, \quad (3)$$

where $\tau \in \{\text{rad}, \text{loss}\}$ and ξ_{τ} accounts for a variable radiative efficiency η (defined as the ratio of radiative to total energy loss): $\xi_{\text{loss}} = 1$ and $\xi_{\text{rad}} = \eta(1 - \eta) \leq 1/4$. Hereafter, we consider isotropic and nonmagnetic materials (and thus a scalar susceptibility χ), but the generalizations to anisotropic and/or magnetic media are straightforward.

Combining Eqs. (2) and (3) yields a general limit on the loss or emission spectral probabilities $\Gamma_{\tau}(\omega) = P_{\tau}(\omega)/\hbar\omega$:

$$\Gamma_{\tau}(\omega) \leq \frac{\alpha \xi_{\tau} c}{2\pi\omega^2} \int_V \frac{|\chi|^2}{\text{Im}\chi} \left[\kappa_{\rho}^4 K_0^2(\kappa_{\rho}\rho) + \kappa_{\rho}^2 k_v^2 K_1^2(\kappa_{\rho}\rho) \right] dV, \quad (4)$$

where α is the fine-structure constant. Equation (4) imposes, *without* solving Maxwell's equations, a maximum rate of photon generation based on the electron velocity β (through k_v and κ_{ρ}), the material composition $\chi(\mathbf{r})$, and the volume V .

The limit in Eq. (4) can be further simplified by removing the shape dependence of V , since the integrand is positive and is thus bounded above by the same integral for any enclosing structure. A scatterer separated from the electron by a

minimum distance d can be enclosed within a larger concentric hollow cylinder sector of inner radius d and outer radius ∞ . For such a sector (height L and opening azimuthal angle $\psi \in [0, 2\pi]$), Eq. (4) can be further simplified, leading to a general closed-form *shape-independent* limit (see Supplementary 2) that highlights the pivotal role of the impact parameter $\kappa_{\rho}d$:

$$\Gamma_{\tau}(\omega) \leq \frac{\alpha \xi_{\tau}}{2\pi c} \frac{|\chi|^2}{\text{Im}\chi} \frac{L\psi}{\beta^2} \left[(\kappa_{\rho}d) K_0(\kappa_{\rho}d) K_1(\kappa_{\rho}d) \right], \quad (5a)$$

$$\propto \frac{1}{\beta^2} \begin{cases} \ln(1/\kappa_{\rho}d) & \text{for } \kappa_{\rho}d \ll 1, \\ \pi e^{-2\kappa_{\rho}d}/2 & \text{for } \kappa_{\rho}d \gg 1. \end{cases} \quad (5b)$$

The limits of Eqs. (4,5) are completely general; they set the maximum photon emission and energy loss of an electron beam coupled to an arbitrary photonic environment in either the nonretarded or retarded regimes, given only the beam properties and material composition. The key factors that determine maximal radiation are identified: intrinsic material loss (represented by $\text{Im}\chi$), electron velocity β , and impact parameter $\kappa_{\rho}d$. The metric $|\chi|^2/\text{Im}\chi$ reflects the influence of the material choice, which depends sensitively on the radiation wavelength [Fig. 1(b)]. The electron velocity β also appears implicitly in the impact parameter $\kappa_{\rho}d = kd/\beta\gamma$, showing that

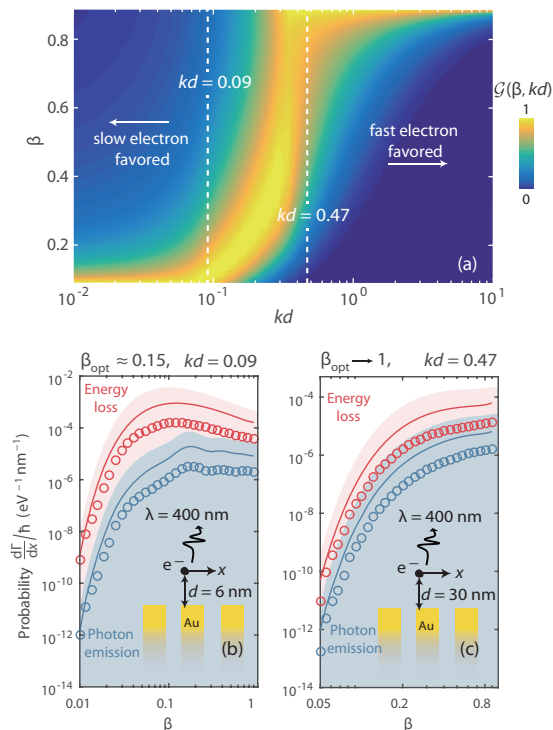


Figure 2. Optimal electron velocities for maximal Smith–Purcell radiation. (a) Behavior of $\mathcal{G}(\beta, kd)$, Eq. (6), whose maxima indicate separation-dependent optimal electron velocities. Here \mathcal{G} is normalized between 0 and 1 for each separation. The limit yields sharply-contrasting predictions: slow electrons are optimal in the near field ($kd \ll 1$) and fast electrons are optimal in the far field ($kd \gg 1$). (b–c) Energy loss (red) and radiation (blue) rates [circles: full-wave simulations; lines: grating limit, Eq. (6); shadings: shape-independent limit, Eq. (5)] at two representative near/far-field separation distances [white dashed slices in (a)].

the relevant length scale is set by the relativistic velocity of the electron. The impact parameter $\kappa_p d$ reflects the influence of the Lorentz contraction d/γ ; a well-known feature of both electron radiation and acceleration [20, 27, 32].

A surprising feature of the limits in Eqs (4,5) is their prediction for optimal electron velocities. As shown in Fig. 1(c), when electrons are in the far field of the structure ($\kappa_p d \gg 1$), stronger photon emission and energy loss are achieved by faster electrons—a well-known result. On the contrary, if electrons are in the near field ($\kappa_p d \ll 1$), *slower* electrons are optimal. This contrasting behavior is evident in the asymptotics of Eq. (5b), where the $1/\beta^2$ or $e^{-2\kappa_p d}$ dependence is dominant at short or large separations. Physically, the optimal velocities are determined by the incident-field properties [Eq. (2)]: slow electrons generate stronger near field amplitudes although they are more evanescent (Supplementary 2). There has been a recent interest in using low-energy electrons for Cherenkov [10] and Smith–Purcell [33] radiation; our prediction that they can be optimal at subwavelength interaction distances underscores the substantial technological potential of nonrelativistic free-electron radiation sources.

The tightness of the limit [Eqs. (4,5)] is demonstrated by comparison with full-wave numerical calculations (see Methods.) in Figs. 1(d–e). Two scenarios are considered: in Fig. 1(d), an electron traverses the center of an annular Au bowtie antenna and undergoes antenna-enabled transition radiation ($\eta \approx 0.07\%$), while, in Fig. 1(e), an electron traverses a Au grating, undergoing Smith–Purcell radiation ($\eta \approx 0.9\%$). In both cases, the numerical results closely trail the upper limit at the considered wavelengths, showing that the limits can be approached or even attained with modest effort.

Next, we specialize in the canonical Smith–Purcell setup illustrated in Fig. 1(e) inset. This setup warrants a particularly close study, given its prominent historical and practical role in free-electron radiation. Aside from the shape-independent limit [Eq. (5)], we can find a sharper limit (in per unit length for periodic structure) specifically for Smith–Purcell radiation using rectangular gratings of filling factor Λ (see Supplementary 3)

$$\frac{d\Gamma_\tau(\omega)}{dx} \leq \frac{\alpha \xi_\tau}{2\pi c} \frac{|\chi|^2}{\text{Im}\chi} \Lambda \mathcal{G}(\beta, kd). \quad (6)$$

The function $\mathcal{G}(\beta, kd)$ is an azimuthal integral (see Supplementary 3) over the Meijer G-function $G_{1,3}^{3,0}$ [28] that arises in the radial integration of the modified Bessel functions K_n . We emphasize that Eq. (6) is a specific case of Eq. (4) for grating structures without any approximations and thus can be readily generalized to multi-material scenarios [see Supplementary Eq. (S37)].

The grating limit [Eq. (6)] exhibits the same asymptotics as Eq. (5), thereby reinforcing the optimal-velocity predictions of Fig. 1(c). The (β, kd) dependence of \mathcal{G} , see Fig. 2(a), shows that slow (fast) electrons maximize Smith–Purcell radiation in the small (large) separation regime. We verify the limit predictions by comparison with numerical simulations: At small separations [Figs. 2(b)], radiation and energy loss peak at velocity $\beta \approx 0.15$, consistent with the limit maximum; at large separations [Figs. 2(c)], both the limit and the numerical results grow monotonically with β .

The derived upper limit also applies to Cherenkov and transition radiation, as well as bulk loss in electron energy loss spectroscopy (EELS). For these scenarios where electrons enter material bulk, a subtlety arises for the field divergence along the electron’s trajectory [$\rho = 0$ in Eq. (2)] within a potentially lossy medium. This divergence, however, can be regularized by introducing natural, system-specific momentum-cutoffs [27], which then directly permits the application of our theory (see Supplementary 6). Meanwhile, there exist additional competing interaction processes (e.g., electrons colliding with individual atoms). However, they typically occur at much smaller length scales.

We perform quantitative experimental measurement of Smith–Purcell radiation to directly probe the upper limit. Fig. 3(a) shows our experimental setup (see Methods and Supplementary 7 for details). A one-dimensional 50%-filling-factor grating (Au-covered single-crystalline Si)—the quintessential Smith–Purcell setup—is chosen as a sample,

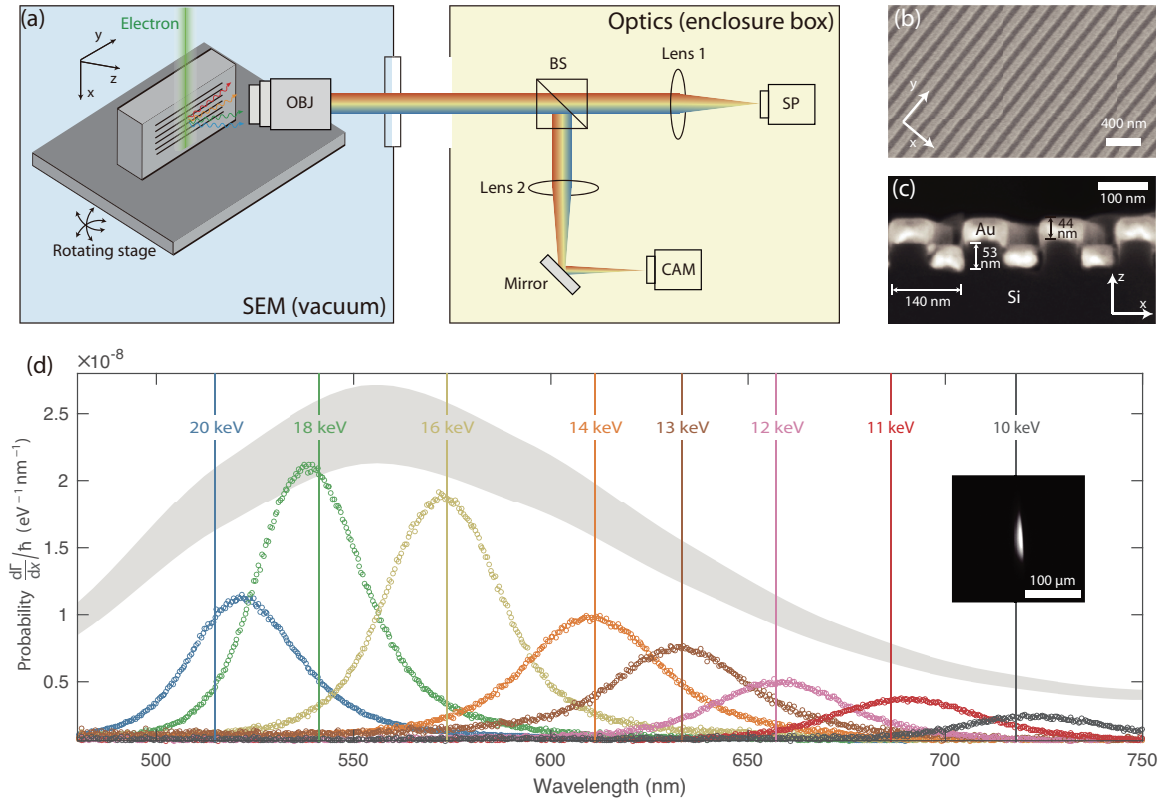


Figure 3. **Experimental probing of the upper limit.** (a) Experimental setup. OBJ, objective ($NA = 0.3$); BS, beam splitter; SP, spectrometer; CAM, camera. (b-c) SEM images of the structure in (b) top view and (c) cross-sectional view. (d) Quantitative measurement of Smith–Purcell radiation (inset: camera image of the radiation). Solid lines mark the theoretical radiation wavelengths at the normal angle [Eq. (1)]. The envelope (peak outline) of the measured spectra (dots) follows the theoretical upper limit (shaded to account for fabrication tolerance; calculated at each wavelength with the corresponding electron velocity for surface-normal radiation).

and shown by SEM images in Figs. 3(b-c). Free electrons pass above and impinge onto the sample at a grazing angle of 1.5° under 10 to 20 kV acceleration voltages.

Fig. 3(d) depicts our measurements of first order $m = 1$ Smith–Purcell radiation appearing at wavelengths between 500 and 750 nm. In quantitative agreement with Eq. (1) evaluated at normal emission angle (solid lines), the measured radiation spectra (dots) blueshift with increasing electron velocity. Notably, we experimentally obtain the absolute intensity of the collected radiation via a calibration measurement (see Supplementary 7). The upper limits [Eq. (4)] for the surface-normal emission wavelengths ($\lambda = a/\beta$) are evaluated at the center of the interaction region [height ≈ 140 nm ($kd \approx 1.5$), varying with beam energy], and is shown with shading in Fig. 3(d) to account for the thickness uncertainty (± 1.5 nm). The envelope spanned by the measurement peaks follows the upper-limit lineshape across the visible spectrum: both the theoretical limit and the measured intensities peak near 550 nm and decrease in a commensurate manner for other wavelengths. This lineshape originates from two competing factors. At shorter wavelengths, the material factor $|\chi^2|/\text{Im}\chi$ decreases significantly for both Au and Si [see Fig. 1(c)], which accounts for the reduced radiation intensity. At longer wavelengths, the major constraint becomes the less efficient

interaction between the electrons and the structure, as the electron-beam diameters increase for the reduced brightness of the electron gun (tungsten) at lower acceleration voltages (see Supplementary 7). These experimental evidences for the upper limit are at $kd \approx 1.5$ (estimated from a geometrical ray-tracing model; see Supplementary 7), where fast electrons are still preferred [Fig. 2(a)]. To further confirm our theory, we also conduct a near-infrared Smith–Purcell experiment (Supplementary 8) at $kd \approx 1$, where the envelope lineshape of the emission spectra again follows our prediction. Additionally, we also obtain complementary supporting evidence (extracted from the data in a recent work [10]) for our slow-electron-efficient prediction (see Supplementary 9).

Finally, we turn our attention to an ostensible peculiarity of the limits: Eq. (4) evidently diverges for lossless materials ($\text{Im}\chi \rightarrow 0$), seemingly providing little insight. On the contrary, this divergence suggests the existence of a mechanism capable of strongly enhancing Smith–Purcell radiation. Indeed, by exploiting high- Q resonances near BICs [13] in photonic crystal slabs, we find that Smith–Purcell radiation can be enhanced by orders of magnitude, when specific frequency, phase, and polarization matching conditions are met.

A one-dimensional silicon ($\chi = 11.25$)-on-insulator (SiO_2 , $\chi = 1.07$) grating interacting with a sheet electron beam il-

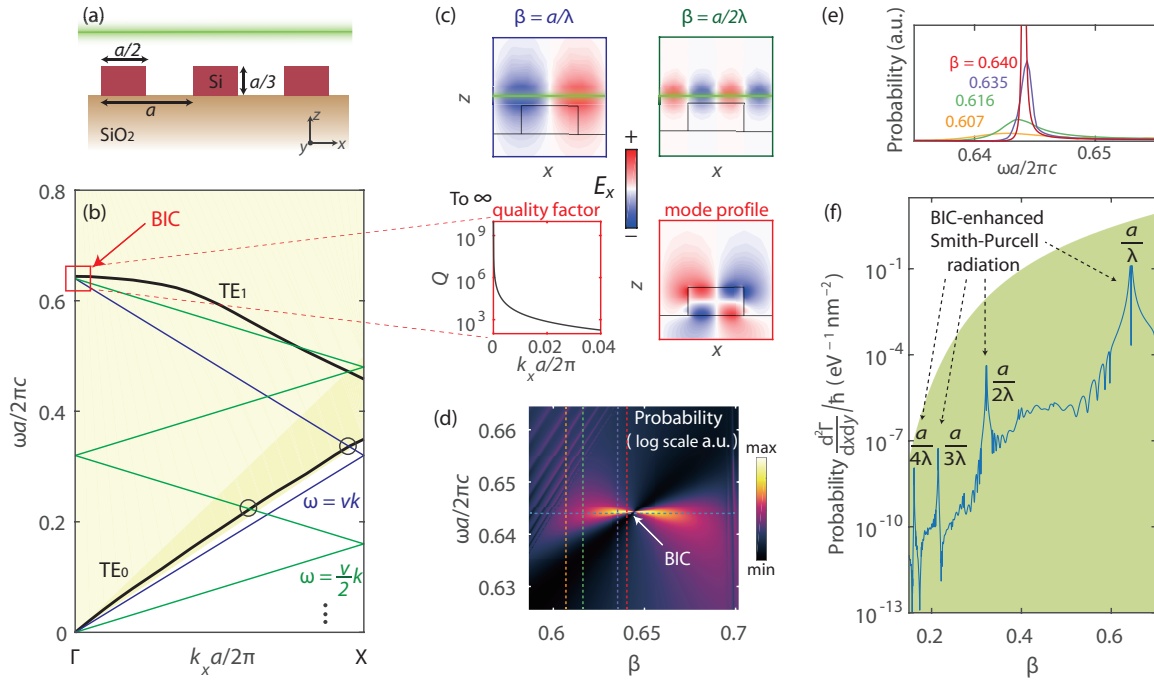


Figure 4. Strong enhancement of Smith–Purcell radiation via high- Q resonances near a photonic bound state in the continuum (BIC). (a) Schematic drawing of a silicon-on-insulator grating (one-dimensional photonic crystal slab: periodic in x and infinite in y). (b) Calculated TE band structure (solid black lines) in the Γ – X direction. The area shaded in light and dark yellow indicates the light cone of air and silica, respectively. The electron lines (blue for velocity v , and green for $v/2$) can phase match with either the guided modes (circles) or high- Q resonances near a BIC (red square). (c) Upper: Incident field of electrons. Lower: resonant quality factors (left) and eigenmode profile (right) near a BIC. (d) Strongly enhanced Smith–Purcell radiation near the BIC. (e) Vertical slices of (d). (f) The limit (shaded area) comparing with the horizontal slice of (d), with material loss considered. Strong enhancement happens at electron velocities $\beta = a/m\lambda$ ($m = 1, 2, 3 \dots$).

illustrates the core conceptual idea most clearly. The transverse electric (TE) (E_x, H_y, E_z) band structure (lowest two bands labeled TE_0 and TE_1), matched polarization for a sheet electron beam [Eq. (S41b)], is depicted in Fig. 4(b) along the Γ – X direction. Folded electron wave vectors, $k_v = \omega/v$, are overlaid for two distinct velocities (blue and green). Strong electron-photon interactions are possible when the electron and photon dispersions intersect: for instance, k_v and the TE_0 band intersect (grey circles) below the air light cone (light yellow shading). However, these intersections are largely impractical: the TE_0 band is evanescent in the air region, precluding free-space radiation. Still, analogous ideas, employing similar partially guided modes, e.g., spoof plasmons [34], have been explored for generating electron-enabled guided waves [35, 36].

To overcome this deficiency, we theoretically propose a new mechanism for enhanced Smith–Purcell radiation: coupling of electrons with BICs [13]. The latter have the extreme quality factors of guided modes but are, crucially, embedded in the radiation continuum, guaranteeing any resulting Smith–Purcell radiation into the far field. By choosing appropriate velocities $\beta = a/m\lambda$ (m any integer; λ the BIC wavelength) such that the electron line (blue or green) intersects the TE_1 mode at the BIC [red square in Fig. 4(b)], the strong enhancements of a guided mode can be achieved in tandem with the radiative coupling of a continuum resonance.

In Fig. 4(c), the incident fields of electrons and the field profile of the BIC indicate their large modal overlaps. The BIC field profile shows complete confinement without radiation, unlike conventional multipolar radiation modes (see Supplementary Fig. S9). The Q s of the resonances are also provided near a symmetry-protected BIC [13] at the Γ point. Figs. 4(d) and (e) demonstrate the velocity tunability of BIC-enhanced radiation—as the phase matching approaches the BIC, a divergent radiation rate is achieved.

The BIC-enhancement mechanism is entirely accordant with our upper limits. Practically, silicon has nonzero loss across the visible and near infrared wavelengths. E.g., for a period of $a = 676$ nm, the optimally enhanced radiation wavelength is ≈ 1050 nm, at which $\chi_{Si} \approx 11.25 + 0.001i$ [37]. For an electron–structure separation of 300 nm, we theoretically show in Fig. 4(f) the strong radiation enhancements (> 3 orders of magnitude) attainable by BIC-enhanced coupling. The upper limit [shaded region; 2D analogue of Eq. (4), see Supplementary 10] attains extremely large values due to the minute material loss ($|\chi|^2/\text{Im}\chi \approx 10^5$); nevertheless, BIC-enhanced coupling enables the radiation intensity to closely approach this limit at several resonant velocities. In the presence of absorptive channel, the maximum enhancement occurs at a small offset from the BIC where the Q -matching condition (see Supplementary 11) is satisfied, i.e., equal ab-

sorptive and radiative rates of the resonances.

In closing, we have theoretically derived and experimentally probed a universal upper limit to the energy loss and photon emission from free electrons. The limit depends crucially on the impact parameter $\kappa_p d$, but *not* on any other detail of the geometry. Hence, our limit applies even to the most complex metamaterials and metasurfaces, given only their constituents. Surprisingly in the near field slow electrons promise stronger radiation than relativistic ones. The limit predicts a divergent radiation rate as the material loss rate goes to zero, and we show that BIC resonances enable such staggering enhancements. This is relevant for the generation of coherent Smith–Purcell radiation [14, 35, 36]. The long lifetime, spectral selectivity, and large field enhancement near a BIC can strongly bunch electrons, allowing them to radiate coherently at the same desired frequency, potentially enabling low-threshold Smith–Purcell free electron lasers. The combination of this mechanism and the optimal velocity prediction reveals prospects of low-voltage yet high-power free-electron radiation sources. In addition, our findings demonstrate a simple guiding principle to maximize the signal-to-noise ratio for EELS through an optimal choice of electron velocity, enabling improved spectral resolution.

The predicted slow-electron-efficient regime still calls for direct experimental validation. We suggest that field-emitter-integrated free-electron devices (e.g. [10]) are ideal to confirm the prediction due to the achievable small electron-structure separation and high electron beam quality at relatively large currents. Additionally, the microwave or Terahertz frequencies could be suitable testing spectral ranges, where the sub-wavelength separation requirement is more achievable.

The upper limit demonstrated here is in the spontaneous emission regime for constant-velocity electrons, and can be extended to the stimulated regime by suitable reformulation. Stronger electron-photon interactions can change electron velocity by a non-negligible amount that alters the radiation. If necessary, this correction can be perturbatively incorporated. In the case of external optical pumping [38], the upper limit can be revised by redefining the incident field as the summation of the electron incident field and the external optical field. From a quantum mechanical perspective, this treatment corresponds to stimulated emission from free electrons, which multiplies the limit by the number of photons in that radiation mode. This treatment could also potentially translate our limit into a fundamental limit for particle acceleration [39, 40], which is the time-reversal of free electron energy loss and which typically incorporates intense laser pumping. In the multi-electron scenario, the radiation upper limit will be obtained in the case of perfect bunching, where all electrons radiate in phase. In this case, our single-electron limit should be multiplied by the number of electrons to correct for the superradiant nature of such coherent radiation.

METHODS

Methods, including statements of data availability and any associated accession codes and references, are available at xxx

* yy@mit.edu

† owen.miller@yale.edu

‡ kaminer@technion.ac.il

-
- [1] P. A. Cherenkov, Dokl. Akad. Nauk SSSR **2**, 451 (1934).
 - [2] S. J. Smith and E. Purcell, Physical Review **92**, 1069 (1953).
 - [3] V. Ginsburg and I. Frank, Zh. Eksp. Teor. Fiz **16**, 15 (1946).
 - [4] P. Goldsmith and J. Jelley, Philos. Mag. **4**, 836 (1959).
 - [5] S. Liu, P. Zhang, W. Liu, S. Gong, R. Zhong, Y. Zhang, and M. Hu, Phys. Rev. Lett. **109**, 153902 (2012).
 - [6] I. Kaminer, Y. T. Katan, H. Buljan, Y. Shen, O. Ilic, J. J. López, L. J. Wong, J. D. Joannopoulos, and M. Soljačić, Nat. Commun. **7** (2016).
 - [7] C. Luo, M. Ibanescu, S. G. Johnson, and J. Joannopoulos, Science **299**, 368 (2003).
 - [8] G. Adamo, K. F. MacDonald, Y. Fu, C. Wang, D. Tsai, F. G. de Abajo, and N. Zheludev, Phys. Rev. Lett. **103**, 113901 (2009).
 - [9] V. Ginis, J. Danckaert, I. Veretennicoff, and P. Tassin, Phys. Rev. Lett. **113**, 167402 (2014).
 - [10] F. Liu, L. Xiao, Y. Ye, M. Wang, K. Cui, X. Feng, W. Zhang, and Y. Huang, Nat. Photon. **11**, 289 (2017).
 - [11] C. W. Hsu, B. Zhen, J. Lee, S.-L. Chua, S. G. Johnson, J. D. Joannopoulos, and M. Soljačić, Nature **499**, 188 (2013).
 - [12] Y. Yang, C. Peng, Y. Liang, Z. Li, and S. Noda, Phys. Rev. Lett. **113**, 037401 (2014).
 - [13] C. W. Hsu, B. Zhen, A. D. Stone, J. D. Joannopoulos, and M. Soljačić, Nat. Rev. Mater. **1**, 16048 (2016).
 - [14] J. Urata, M. Goldstein, M. Kimmitt, A. Naumov, C. Platt, and J. Walsh, Phys. Rev. Lett. **80**, 516 (1998).
 - [15] S. Korbly, A. Kesar, J. Sirigiri, and R. Temkin, Phys. Rev. Lett. **94**, 054803 (2005).
 - [16] G. Doucas, J. Mulvey, M. Otori, J. Walsh, and M. Kimmitt, Phys. Rev. Lett. **69**, 1761 (1992).
 - [17] G. Kube, H. Backe, H. Euteneuer, A. Grendel, F. Hagenbuck, H. Hartmann, K. Kaiser, W. Lauth, H. Schöpe, G. Wagner, T. Walcher, and M. Kretzschmar, Phys. Rev. E **65**, 056501 (2002).
 - [18] N. Yamamoto, F. J. G. de Abajo, and V. Myroshnychenko, Phys. Rev. B **91**, 125144 (2015).
 - [19] I. Kaminer, S. Kooi, R. Shiloh, B. Zhen, Y. Shen, J. López, R. Remez, S. Skirlo, Y. Yang, J. Joannopoulos, and M. Soljačić, Phys. Rev. X **7**, 011003 (2017).
 - [20] M. J. Moran, Phys. Rev. Lett. **69**, 2523 (1992).
 - [21] P. Van den Berg, JOSA **63**, 1588 (1973).
 - [22] O. Haeberlé, P. Rullhusen, J.-M. Salomé, and N. Maene, Phys. Rev. E **49**, 3340 (1994).
 - [23] D. Y. Sergeeva, A. Tishchenko, and M. Strikhanov, Phys. Rev. ST Accel. Beams **18**, 052801 (2015).
 - [24] J. Pendry and L. Martin-Moreno, Phys. Rev. B **50**, 5062 (1994).
 - [25] F. G. de Abajo, Phys. Rev. E **61**, 5743 (2000).
 - [26] E. D. Palik, *Handbook of optical constants of solids*, Vol. 3 (Academic press, 1998).
 - [27] F. G. De Abajo, Rev. Mod. Phys. **82**, 209 (2010).
 - [28] M. Abramowitz and I. A. Stegun, *Handbook of mathematical functions: with formulas, graphs, and mathematical tables*,

- Vol. 55 (Courier Corporation, 1964).
- [29] O. D. Miller, A. G. Polimeridis, M. H. Reid, C. W. Hsu, B. G. DeLacy, J. D. Joannopoulos, M. Soljačić, and S. G. Johnson, *Opt. Express* **24**, 3329 (2016).
 - [30] Y. Yang, O. D. Miller, T. Christensen, J. D. Joannopoulos, and M. Soljačić, *Nano Lett.* **17**, 3238 (2017).
 - [31] O. D. Miller, S. G. Johnson, and A. W. Rodriguez, *Phys. Rev. Lett.* **115**, 204302 (2015).
 - [32] A. Friedman, A. Gover, G. Kurizki, S. Ruschin, and A. Yariv, *Reviews of modern physics* **60**, 471 (1988).
 - [33] A. Massuda, C. Roques-Carnes, Y. Yang, S. E. Kooi, Y. Yang, C. Murdia, K. K. Berggren, I. Kaminer, and M. Soljačić, arXiv preprint arXiv:1710.05358 (2017).
 - [34] J. Pendry, L. Martin-Moreno, and F. Garcia-Vidal, *Science* **305**, 847 (2004).
 - [35] H. Andrews and C. Brau, *Phys. Rev. ST Accel. Beams* **7**, 070701 (2004).
 - [36] V. Kumar and K.-J. Kim, *Phys. Rev. E* **73**, 026501 (2006).
 - [37] M. A. Green, *Sol. Energy Mater. Sol. Cells* **92**, 1305 (2008).
 - [38] L. Schächter and A. Ron, *Phys. Rev. A* **40**, 876 (1989).
 - [39] E. A. Peralta, K. Soong, R. England, E. R. Colby, Z. Wu, B. Montazeri, C. McGuinness, J. McNeur, K. J. Leedle, D. Walz, E. B. Sozer, B. Cowan, B. Schwartz, G. Travish, and R. L. Byer, *Nature* **503**, 91 (2013).
 - [40] J. Breuer and P. Hommelhoff, *Phys. Rev. Lett.* **111**, 134803 (2013).

ACKNOWLEDGEMENTS

The authors thank fruitful discussions with Prof. Shouzhi Yang, Prof. Chao Peng, Prof. Avi Gover, Prof. Bo Zhen, Dr. Liang Jie Wong, Dr. Xiao Lin, Di Zhu, Tena Dubcek, and Nicholas Rivera. We thank Dr. Paola Rebusco for critical reading and editing of the manuscript. This work was per-

formed in part at the Harvard University Center for Nanoscale Systems (CNS), a member of the National Nanotechnology Coordinated Infrastructure Network (NNCI), which is supported by the National Science Foundation under NSF ECCS award no. 1541959. This work was partly supported by the Army Research Office through the Institute for Soldier Nanotechnologies under contract No. W911NF-18-2-0048 and W911NF-13-D-0001. Y.Y. was partly supported by the MR-SEC Program of the National Science Foundation under Grant No. DMR-1419807. T.C. was supported by the Danish Council for Independent Research (Grant No. DFFC6108-00667). O.D.M. was supported by the Air Force Office of Scientific Research under award number FA9550-17-1-0093. I.K. was partially supported by the Seventh Framework Programme of the European Research Council (FP7- Marie Curie IOF) under grant agreement No. 328853CMC-BSiCS.

AUTHOR CONTRIBUTIONS

Y.Y., O.D.M., I.K., and M.S. conceived the project. Y.Y. developed the analytical models and numerical calculations. A.M. prepared the sample under study. Y.Y., A.M., C.R.-C., S.E.K., and I.K. performed the experiment. Y.Y., T.C., and O.D.M. analyzed the asymptotics and bulk loss of the limit. S.G.J., J.D.J., O.D.M., I.K., and M.S. supervised the project. Y.Y. wrote the manuscript with inputs from all authors.

COMPETING INTERESTS

The authors declare no competing interests.

SUPPLEMENTARY INFORMATION

Maximal Spontaneous Photon Emission and Energy Loss from Free Electrons

Yi Yang^{1,*}, Aviram Massuda¹, Charles Roques-Carmes¹, Steven E. Kooi²,
Thomas Christensen¹, Steven G. Johnson¹, John D. Joannopoulos^{1,2},
Owen D. Miller^{3,†}, Ido Kaminer^{1,4,‡} and Marin Soljačić¹

¹*Research Laboratory of Electronics, Massachusetts Institute of Technology, Cambridge, Massachusetts 02139, USA*

²*Institute for Soldier Nanotechnologies, 77 Massachusetts Avenue, Cambridge, Massachusetts 02139, USA*

³*Department of Applied Physics & Energy Sciences Institute,
Yale University, New Haven, CT 06520, USA and*

⁴*Andrew & Erna Viterbi Department of Electrical Engineering,
Technion-Israel Institute of Technology, 32000 Haifa, Israel*

* yyi@mit.edu

† owen.miller@yale.edu

‡ kaminer@technion.ac.il

1. GENERAL OPTICAL RESPONSE LIMIT FRAMEWORK

Intuitively, to impose the general limits on the energy loss and photon emission (cathodoluminescence) from free electrons, we consider an arbitrary scatterer embedded in a possibly heterogeneous background. Passivity, which implies the absence of gain and that polarization currents do no work [1] requires that the absorbed (P_{abs}) and scattered (P_{rad}) powers by the target body are non-negative. On the other hand, their sum, the electron energy loss ($P_{\text{loss}} = P_{\text{abs}} + P_{\text{rad}}$), is given by the real part of the overlap between the electron velocity and the induced field [2], similar to the optical theorem [3].

More broadly, for an arbitrarily shaped 3D scatterer [volume V and susceptibility tensor $\overline{\overline{\chi}}(\mathbf{r}, \omega)$] impinged by the external incident field $\mathbf{F}_{\text{inc}} = (\mathbf{E}_{\text{inc}}, Z_0 \mathbf{H}_{\text{inc}})^T$ [for the case of free electrons, see Eq. (2)], the absorption (dissipation) within such a medium is the work done by the total fields \mathbf{F} on the induced currents, given by the expression

$$P_{\text{abs}} = \frac{\epsilon_0 \omega}{2} \text{Im} \int_V \mathbf{F}^\dagger \overline{\overline{\chi}} \mathbf{F} dV. \quad (\text{S1})$$

On the other hand, the total electron energy loss represents the work done by the incident fields on the induced currents

$$P_{\text{loss}} = \frac{\epsilon_0 \omega}{2} \text{Im} \int_V \mathbf{F}_{\text{inc}}^\dagger \overline{\overline{\chi}} \mathbf{F} dV. \quad (\text{S2})$$

As can be seen, Electron total energy loss and absorption are linear and quadratic function of the fields, respectively. Yet electron energy loss must be greater than absorption (due to the nonnegative scattering noted above), requiring the linear functional to be greater than the quadratic one, a condition that cannot be satisfied for large enough currents. The inequality $P_{\text{abs}} \leq P_{\text{loss}}$ thereby provides a convex constraint for the optical excitation of free electrons. Thanks to the convex nature of the constraint $P_{\text{abs}} \leq P_{\text{loss}}$ and the simple expressions of the absorption and energy loss, the optimal response can be solved analytically using variational derivatives, without the requirement of solving the highly nonconvex Maxwell equations, thereby providing general upper-limit expressions for electron energy loss and photon emission without approximation.

To obtain the extremum induced fields/currents for electron energy loss or photon emission (cathodoluminescence), one can take the derivative $\frac{\partial P_\tau(\omega)}{\partial \mathbf{F}^\dagger} = 0$, where $\tau \in \{\text{rad}, \text{loss}\}$. Using the photon emission as an example, by taking

$$\frac{\partial P_{\text{rad}}(\omega)}{\partial \mathbf{F}^\dagger} = \frac{\partial (P_{\text{loss}} - P_{\text{abs}})}{\partial \mathbf{F}^\dagger} = 0, \quad (\text{S3})$$

we have

$$\bar{\chi}^\dagger \mathbf{F}_{\text{inc}}/2i + (\text{Im}\bar{\chi})\mathbf{F} = 0, \quad (\text{S4})$$

where $\text{Im}\bar{\chi} = (\bar{\chi} - \bar{\chi}^\dagger)/2i$ is a Hermitian matrix. From Eq. (S4), one readily finds the optimal total field is given by $\mathbf{F}_{\text{rad,opt}} = \frac{i}{2}(\text{Im}\bar{\chi})^{-1}\bar{\chi}^\dagger \mathbf{F}_{\text{inc}}$. The optimal field for maximal electron energy loss can be derived in a similar manner. Combining the optimal fields with Eq. (S1) and Eq. (S2), we obtain the upper limit shown in Eq. (3) in the main text.

2. THREE-DIMENSIONAL SHAPE-INDEPENDENT UPPER LIMIT

We first rewrite the three-dimensional general limit equation

$$\Gamma_\tau(\omega) \leq \frac{e^2\xi_\tau}{8\hbar\epsilon_0\omega^2\pi^2} \int_V \frac{|\chi|^2}{\text{Im}\chi} \left[\kappa_\rho^4 K_0^2(\kappa_\rho\rho) + \kappa_\rho^2 k_v^2 K_1^2(\kappa_\rho\rho) \right] dV. \quad (\text{S5})$$

We assume the structure is made of a single material

$$\Gamma_\tau(\omega) \leq \frac{e^2\xi_\tau}{8\hbar\epsilon_0\omega^2\pi^2} \frac{|\chi|^2}{\text{Im}\chi} \int_V \left[\kappa_\rho^4 K_0^2(\kappa_\rho\rho) + \kappa_\rho^2 k_v^2 K_1^2(\kappa_\rho\rho) \right] dV. \quad (\text{S6})$$

We now simplify the integral

$$\mathcal{K} = \int_V \left[\kappa_\rho^4 K_0^2(\kappa_\rho\rho) + \kappa_\rho^2 k_v^2 K_1^2(\kappa_\rho\rho) \right] dV. \quad (\text{S7})$$

For an arbitrarily-shaped structure, whether isolated or extended, one can always find a circular concentric hollow cylinder (height L , opening azimuthal angle $\psi \in [0, 2\pi]$, minor radius being the electron structure separation, major radius can be finite or infinite) that encloses it. Therefore, we can evaluate the integral in the cylindrical coordinate

$$\begin{aligned} \mathcal{K} &\leq L\psi \int_d^\infty \rho \left[\kappa_\rho^4 K_0^2(\kappa_\rho\rho) + \kappa_\rho^2 k_v^2 K_1^2(\kappa_\rho\rho) \right] d\rho \\ &= L\psi \int_{x_0}^\infty x \left[\kappa_\rho^2 K_0^2(x) + k_v^2 K_1^2(x) \right] dx, \\ &= \frac{x_0^2}{2} \left\{ \kappa_\rho^2 \left[K_1^2(x_0) - K_0^2(x_0) \right] + k_v^2 \left[K_0(x_0)K_2(x_0) - K_1^2(x_0) \right] \right\}, \\ &= \frac{x_0^2}{2} \left\{ k_v^2 K_0(x_0) \left[K_2(x_0) - K_0(x_0) \right] - k^2 \left[K_1^2(x_0) - K_0^2(x_0) \right] \right\}, \\ &= x_0 k_v^2 K_0(x_0) K_1(x_0) - x_0^2 k^2 \left[K_1^2(x_0) - K_0^2(x_0) \right], \\ &\leq x_0 k_v^2 K_0(x_0) K_1(x_0), \end{aligned} \quad (\text{S8})$$

where $x_0 = \kappa_\rho d$. Eq. (S8) corresponds to Eq. (5a) in the maintext. In the derivation above, we use the following relations [4]

$$\int x K_n^2(x) dx = \frac{x^2}{2} [K_n^2(x) - K_{n-1}(x)K_{n+1}(x)], \quad (\text{S9a})$$

$$K_{-1}(x) = K_1(x), \quad (\text{S9b})$$

$$K_2(x) - K_0(x) = 2K_1(x)/x, \quad (\text{S9c})$$

$$K_1(x) > K_0(x). \quad (\text{S9d})$$

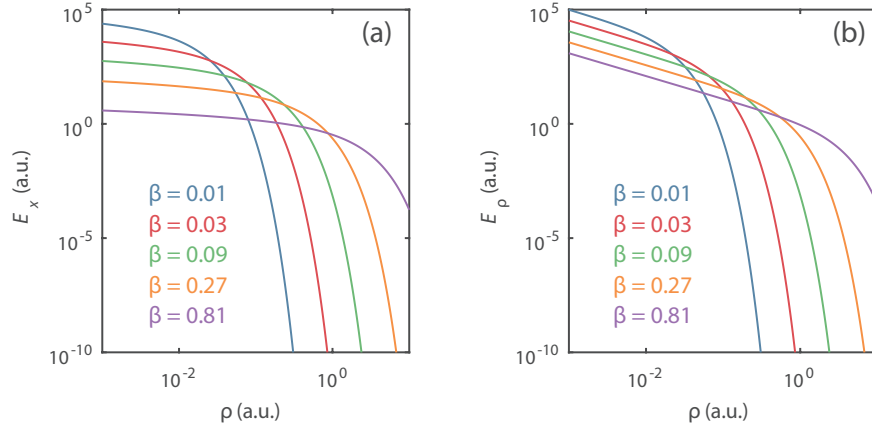


Figure S1. (a) Longitudinal E_x and (b) transverse E_ρ incident field amplitudes generated from free electrons in the azimuthal direction ρ at different velocities β .

In the main text, the shape-independent limit has sharply-contrasting prediction on the intensity of luminescence and energy loss of free electrons when they are in either the far or near field [Eq. (5b)]. Fig. S1 shows that the incident fields already exhibit similar property, which naturally translates into the upper limit via the overlap integral [Eq. (4)].

3. SMITH-PURCELL RADIATION UPPER LIMIT IN THREE DIMENSIONS FOR RECTANGULAR GRATINGS

We choose coordinates such that (vt, y_0, z_0) depicts the trajectory of the charged particle. In the cylindrical coordinate (ρ, ψ, x) , the current density can be rewritten as

$$\mathbf{J}(\mathbf{r}, t) = \frac{-ev}{2\pi\rho} \delta(x - vt) \delta(\rho) \hat{\mathbf{x}}. \quad (\text{S10})$$

Fourier transform on Eq. (S10) yields the current density in the frequency domain

$$\mathbf{J}(\mathbf{r}, \omega) = \frac{-e}{2\pi\rho} e^{ik_v x} \delta(\rho) \hat{\mathbf{x}}, \quad (\text{S11})$$

whose external electromagnetic field is given by [5]

$$\begin{aligned} \mathbf{E}_{\text{inc}}(\mathbf{r}, \omega) &= \frac{e}{4\omega\epsilon_0} (k^2 \hat{\mathbf{x}} + ik_v \nabla) H_0^{(1)}(i\kappa_\rho \rho) e^{ik_v x}, \\ &= \frac{e}{4\omega\epsilon_0} [(k^2 - k_v^2) H_0^{(1)}(i\kappa_\rho \rho) \hat{\mathbf{x}} + ik_v d_\rho H_0^{(1)}(i\kappa_\rho \rho) \hat{\rho}] e^{ik_v x}, \\ &= \frac{e}{2\pi\omega\epsilon_0} [i\kappa_\rho^2 K_0(\kappa_\rho \rho) \hat{\mathbf{x}} - \kappa_\rho k_v K_1(\kappa_\rho \rho) \hat{\rho}] e^{ik_v x}. \end{aligned} \quad (\text{S12})$$

where $H_0^{(1)}$ is the Hankel function of the first kind with zero order. Here we utilize the relation $K_0(z) = \frac{i\pi}{2} H_0^{(1)}(iz)$, where z is a real argument. Insert Eq. (S12) into Eq. (3) yields the general three-dimensional limit shown in Eq. (4).

Next we consider Smith–Purcell radiation from rectangular gratings in three dimensions. The volume integral of the evanescent field is given by

$$\int_V |\mathbf{E}(\mathbf{r})|^2 dV = \frac{e^2}{4\omega^2 \epsilon_0^2 \pi^2} \int dx \int_{-\pi/2}^{\pi/2} d\psi \int_{d/\cos\psi}^{\infty} \rho d\rho [\kappa_\rho^4 K_0^2(\kappa_\rho \rho) + \kappa_\rho^2 k_v^2 K_1^2(\kappa_\rho \rho)]. \quad (\text{S13})$$

Closed-form integral can be obtained by using the relation

$$\int_{d/\cos\psi}^{\infty} \rho d\rho K_0^2(\kappa_\rho \rho) = \frac{\sqrt{\pi}}{4\kappa_\rho^2} G_{1,3}^{3,0}(\kappa_\rho^2 d^2 \sec^2 \psi |_{0,1,1}), \quad (\text{S14})$$

and

$$\int_{d/\cos\psi}^{\infty} \rho d\rho K_1^2(\kappa_\rho \rho) = \frac{\sqrt{\pi}}{4\kappa_\rho^2} G_{1,3}^{3,0}(\kappa_\rho^2 d^2 \sec^2 \psi |_{0,0,2}). \quad (\text{S15})$$

Here G is the Meijer G-function [4, 6] defined as a line integral in the complex plane

$$G_{p,q}^{m,n} \left(z \mid \begin{matrix} a_1, \dots, a_p \\ b_1, \dots, b_q \end{matrix} \right) = \frac{1}{2\pi i} \int_L \frac{\prod_{j=1}^m \Gamma(b_j - s) \prod_{j=1}^n \Gamma(1 - a_j + s)}{\prod_{j=m+1}^q \Gamma(1 - b_j + s) \prod_{j=n+1}^p \Gamma(a_j - s)} z^s ds, \quad (\text{S16})$$

where Γ is the gamma function.

Plug Eq. (S14) and Eq. (S15) into Eq. (4) yields Eq. (6) in the main text

$$\frac{d\Gamma_\tau(\omega)}{dx} \leq \frac{\alpha \xi_\tau}{2\pi c} \frac{|\chi|^2}{\text{Im}\chi} \Lambda \mathcal{G}(\beta, kd), \quad (\text{S17a})$$

where

$$\mathcal{G}(\beta, kd) = \mathcal{G}_x(\beta, kd) + \mathcal{G}_\rho(\beta, kd), \quad (\text{S17b})$$

$$\mathcal{G}_x(\beta, kd) = \frac{\sqrt{\pi}}{4} \int_{-\pi/2}^{\pi/2} \frac{d\psi}{\beta^2 \gamma^2} G_{3,0}^{1,3} \left(\frac{k^2 d^2}{\beta^2 \gamma^2} \sec^2 \psi \mid_{0,1,1} \right), \quad (\text{S17c})$$

$$\mathcal{G}_\rho(\beta, kd) = \frac{\sqrt{\pi}}{4} \int_{-\pi/2}^{\pi/2} \frac{d\psi}{\beta^2} G_{3,0}^{1,3} \left(\frac{k^2 d^2}{\beta^2 \gamma^2} \sec^2 \psi \mid_{0,0,2} \right). \quad (\text{S17d})$$

Here, $k_v = \omega/c\beta$, $\kappa_\rho = \omega/c\beta\gamma$, and $\alpha = e^2/4\pi\epsilon_0\hbar c$.

4. MAXIMUM OF SMITH–PURCELL RADIATION LIMIT

In Fig. 2, we discuss the limit of Smith–Purcell radiation at a given wavelength as a function of electron velocity. The electron velocity at which the limit of Smith–Purcell radiation achieves maximum corresponds to the zero of its derivative to velocity. In Eq. (4), since the integrand $\kappa_\rho^4 K_0^2(\kappa_\rho \rho) + \kappa_\rho^2 k_v^2 K_1^2(\kappa_\rho \rho)$ is continuous and differentiable, based on the Lagrange’s mean value theorem, there must exist some ρ_0 such that $\int_V \kappa_\rho^4 K_0^2(\kappa_\rho \rho) + \kappa_\rho^2 k_v^2 K_1^2(\kappa_\rho \rho) dV = [\kappa_\rho^4 K_0^2(\kappa_\rho \rho_0) + \kappa_\rho^2 k_v^2 K_1^2(\kappa_\rho \rho_0)] V$. Therefore,

$$\begin{aligned} \frac{d\Gamma(\omega)}{d\beta} &\propto \frac{d\Gamma(\omega)}{d\kappa_\rho} \frac{d\kappa_\rho}{d\beta} \propto \frac{d\Gamma(\omega)}{d\kappa_\rho} \\ &\propto 4\kappa_\rho^3 K_0^2(\kappa_\rho \rho_0) - (3\kappa_\rho^4 \rho_0 + \kappa_\rho^2 k^2 \rho_0) K_0(\kappa_\rho \rho_0) K_1(\kappa_\rho \rho_0) \\ &\quad + (4\kappa_\rho^3 + 2\kappa_\rho k^2) K_1^2(\kappa_\rho \rho_0) - \rho_0 \kappa_\rho^2 (\kappa_\rho^2 + k^2) K_1(\kappa_\rho \rho_0) K_2(\kappa_\rho \rho_0). \end{aligned} \quad (\text{S18})$$

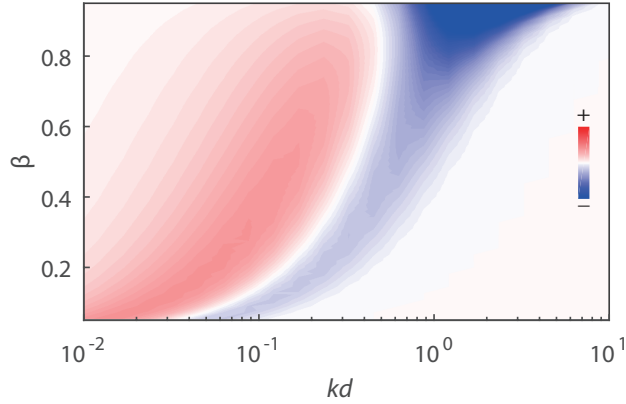


Figure S2. Plot of $\left. \frac{d^2 N(\omega)}{d\omega d\beta} \right|_{\rho_0=2d}$. There is a nodal line of zero derivative that coincides with the limit maximum in Fig. 2.

Fig. S2 is calculated using Eq. S18 where a nodal line of zero derivative appears and coincides with the limit maximum shown in Fig. 2(a), which is consistent with our prediction of optimal velocities as a function of kd .

5. LIMIT ASYMPTOTICS

For the asymptotic behavior of the limit, here we consider four scenarios: electrons in the near field ($kd \rightarrow 0$), electrons in the far field ($kd \rightarrow \infty$), extreme nonrealistic electrons ($v \rightarrow 0$), and

extreme relativistic electrons ($v \rightarrow c$). In this section we only consider the three-dimensional problem [Eq. (4)].

First, we consider near field $kd \rightarrow 0$. We also assume the electron speed is intermediate so neither $\beta \rightarrow 0$ (extremely slow) nor $\gamma \rightarrow \infty$ (extremely fast), which we will discuss later. In the expression of the general limit [Eq. (4)], there are two terms in the integrand where the first term (containing K_0) is the contribution from the longitudinal polarization E_x and the second term (containing K_1) is the contribution from the transverse polarization E_ρ . The hyperbolic Bessel functions K_ν in these two terms has the same argument $\kappa_\rho \rho = k\rho/\beta\gamma$, which also approaches zero for $\rho \gtrsim d$. Both $K_0(\kappa_\rho \rho)$ and $K_1(\kappa_\rho \rho)$ diverge when $\kappa_\rho \rho \rightarrow 0$ but at different divergence rates [4]:

$$\lim_{\rho \rightarrow 0} K_0(\kappa_\rho \rho) \sim -\ln(\kappa_\rho \rho/2) - \gamma_0, \quad (\text{S19a})$$

$$\lim_{\rho \rightarrow 0} K_1(\kappa_\rho \rho) \sim \frac{1}{\kappa_\rho \rho}, \quad (\text{S19b})$$

where γ_0 is the Euler–Mascheroni constant. Therefore, $K_1(\kappa_\rho \rho) \gg K_0(\kappa_\rho \rho)$ when $\kappa_\rho \rho \rightarrow 0$ and E_ρ has the major contribution to the limit.

Second, we consider electron beams in the far field $kd \rightarrow \infty$:

$$\lim_{\rho \rightarrow \infty} K_0(\kappa_\rho \rho) \sim \sqrt{\frac{\pi}{2\kappa_\rho \rho}} e^{-\kappa_\rho \rho} \left[1 - \frac{1}{8\kappa_\rho \rho} + \mathcal{O}(\kappa_\rho^2 \rho^2) \right], \quad (\text{S20a})$$

$$\lim_{\rho \rightarrow \infty} K_1(\kappa_\rho \rho) \sim \sqrt{\frac{\pi}{2\kappa_\rho \rho}} e^{-\kappa_\rho \rho} \left[1 + \frac{3}{8\kappa_\rho \rho} + \mathcal{O}(\kappa_\rho^2 \rho^2) \right]. \quad (\text{S20b})$$

Therefore, both E_x –limit and E_ρ –limit decay exponentially at the same rate and E_ρ –limit remains be higher.

Third, we consider asymptotic behavior of the limit when the electrons are extremely nonrelativistic ($\beta \rightarrow 0$). In this limit, we have $\lim_{\beta \rightarrow 0} \kappa_\rho = k_v \rightarrow \infty$. Thus in Eq. (4)

$$\lim_{\kappa_\rho \rightarrow \infty} \kappa_\rho^2 K_0(\kappa_\rho \rho) \sim \sqrt{\frac{\pi}{2\kappa_\rho \rho}} \kappa_\rho^2 e^{-\kappa_\rho \rho} \left[1 - \frac{1}{8\kappa_\rho \rho} + \mathcal{O}(\kappa_\rho^2 \rho^2) \right] = 0, \quad (\text{S21a})$$

$$\lim_{\kappa_\rho \rightarrow \infty} \kappa_\rho k_v K_1(\kappa_\rho \rho) \sim \sqrt{\frac{\pi}{2\kappa_\rho \rho}} \kappa_\rho^2 e^{-\kappa_\rho \rho} \left[1 + \frac{3}{8\kappa_\rho \rho} + \mathcal{O}(\kappa_\rho^2 \rho^2) \right] = 0, \quad (\text{S21b})$$

which is consistent with the fact that static charges do not generate radiation. Our computational verification is shown in Fig. 2(b) and (c) where both the limit and numerical results approach zero as $\beta \rightarrow 0$ for either small or large separations (whether slow or fast electrons are preferred) between the electron beams and the structure.

Last, we consider the limit behavior when the electrons are extremely relativistic, where $\lim_{\beta \rightarrow 1} \kappa_\rho = \sqrt{\omega^2/v^2 - \omega^2/c^2} = 0$:

$$\lim_{\kappa_\rho \rightarrow 0} \kappa_\rho^2 K_0(\kappa_\rho \rho) \sim \kappa_\rho^2 \left[-\ln(\kappa_\rho \rho/2) - \gamma_0 \right] = 0, \quad (\text{S22a})$$

$$\lim_{\kappa_\rho \rightarrow 0} \kappa_\rho k_v K_1(\kappa_\rho \rho) \sim \kappa_\rho k_v / \kappa_\rho \rho = k_v / \rho. \quad (\text{S22b})$$

Therefore, in this limit, E_x contribution vanishes but E_ρ remains finite. The entire problem becomes equivalent to a plane-wave scattering problem since the incident field is purely transverse.

6. PENETRATING ELECTRON TRAJECTORIES

In the main text, we discuss electron trajectories *near* photonic structures. For *penetrating* electron trajectories—that is, when the electron trajectory $\mathbf{r}_e(t)$ intersects $\chi(\mathbf{r}) \neq 0$ regions—a subtlety arises: the limit, Eq. (3), then apparently diverges even in lossy materials $\text{Im}\chi \neq 0$. In specific terms, the norm-squared incident field \mathbf{E}_{inc} is non-integrable over the electron trajectory, that is $\int_V dV |\mathbf{E}_{\text{inc}}(\mathbf{r})|^2 \sim \int_V dV |\hat{\mathbf{x}} \kappa_\rho \ln \kappa_\rho \rho + \hat{\rho} \gamma \rho^{-1}|^2$ diverges if V includes regions where $\rho = 0$. Here, we discuss the regularization of this divergence with emphasis on the implications to electron energy loss spectroscopy (EELS).

Though at first sight disconcerting, the divergence is not a surprise: the direct calculation of the EEL spectrum, $\Gamma(\boldsymbol{\rho}, \omega) = \frac{e^2}{\pi \hbar \omega} \text{Re} \int_{-\infty}^{\infty} dx E_x(\boldsymbol{\rho} + x \hat{\mathbf{x}}, \omega) e^{-ik_v z}$, is also divergent for penetrating trajectories when $\text{Im}\chi \neq 0$. For an extended bulk material, of permittivity $\epsilon = 1 + \chi$, the EEL spectrum (per unit length L) can be evaluated from the momentum-space representation of the total field (to be introduced shortly), yielding [2]:

$$\Gamma_{\text{EELS}}(\omega) = \frac{e^2 L}{\pi \hbar v^2} \text{Im} \left[\left(\frac{v}{c} - \frac{1}{\epsilon} \right) \ln \left(\frac{q_c^2 + k_v^2 - \epsilon k^2}{k_v^2 - \epsilon k^2} \right) \right]. \quad (\text{S23})$$

The denominator of the logarithm describes the emergence of Cherenkov losses for $v > c/\epsilon$ and is finite—in contrast, the numerator, which describes EEL due to material loss, diverges logarithmically in a momentum cut-off q_c . Of course, the divergence is merely an artifact of an idealized description of the system—several physical and practical considerations impose natural momentum cut-offs, e.g.:

Collection angle: The collection semi-angle of the microscope's spectrometer φ restricts momentum transfer collection to in-plane momenta $q_\rho < q_c$, with $\hbar q_c = m_e v \sin \varphi \simeq m_e v \varphi$. At typ-

ical collection semi-angles and acceleration voltages—say, $\varphi = 10$ mrad and 100 keV—this sets a cut-off at $\hbar q_c \approx 2.8 \times 10^3$ eV/c, or equivalently, a spatial spread $1/q_c \sim 1$ Å.

Nonlocality: Nonlocality effectively suppresses the dielectric response to large-momentum plane-wave components, i.e., $\epsilon(q, \omega) \rightarrow 1$ for $q \gg 1/a$ (lattice constant a). The free-electron response is quenched even earlier, at a threshold set by the Thomas–Fermi momentum.

Electron spread: The spread, ΔR , of the electron’s in-plane density imposes a cut-off $q_c \sim 1/\Delta R$.

To summarize; the divergence of the limit for penetrating trajectories is simply the mirror of the divergence of the direct calculation. Accordingly, the divergence’s remedy is also mirrored: the limit is regularized upon introducing a momentum cut-off in the electron’s (incident) field \mathbf{E}_{inc} . Denoting this regularized field $\mathbf{E}_{\text{inc}, q_c}$, we next verify that this field is indeed regular as $\rho \rightarrow 0$. Coincidentally, this also outlines the derivation of the conventional, non-regularized field [Eq. (2)].

The derivation proceeds as follows: in momentum-frequency space, the electron charge density $\rho(\mathbf{r}, t) = -e\delta(\mathbf{r} - \mathbf{v}t)$ equals $\rho(\mathbf{q}, \omega) = -2\pi e\delta(\omega - \mathbf{q} \cdot \mathbf{v})$ and is accompanied by a current density $\mathbf{J}(\mathbf{q}, \omega) = -2\pi e\mathbf{v}\delta(\omega - \mathbf{q} \cdot \mathbf{v})$. Jointly with Maxwell’s equations, in the form of the wave-equation $(q^2 - \epsilon k^2)\mathbf{E}_{\text{inc}} = i\epsilon_0^{-1}(\mathbf{J}k/c - \rho\mathbf{q}/\epsilon)$, this gives the associated electric field’s (\mathbf{q}, ω) -representation:

$$\mathbf{E}_{\text{inc}}(\mathbf{q}, \omega) = -\frac{2\pi i e}{\epsilon_0} \frac{k\mathbf{v}/c - \mathbf{q}/\epsilon}{q^2 - \epsilon k^2} \delta(\omega - \mathbf{q} \cdot \mathbf{v}). \quad (\text{S24})$$

An inverse transform then yields the (\mathbf{r}, ω) -representation (specializing to $\mathbf{v} = v\hat{\mathbf{x}}$ and $\epsilon = 1$):

$$\begin{aligned} \mathbf{E}_{\text{inc}, q_c}(\mathbf{r}, \omega) &= -\frac{2\pi i e}{\epsilon_0} \int_{|\mathbf{q}| < q_c} \frac{d^3 \mathbf{q}}{(2\pi)^3} \frac{k\mathbf{v}/c - \mathbf{q}}{q^2 - k^2} \delta(\omega - \mathbf{v} \cdot \mathbf{q}) e^{i\mathbf{q} \cdot \mathbf{r}} \\ &= -\frac{i e}{\epsilon_0 v} e^{ik_v x} \int_{|\mathbf{q}_\rho| < q_c} \frac{d^2 \mathbf{q}_\rho}{(2\pi)^2} \frac{(k\mathbf{v}/c - k_v)\hat{\mathbf{x}} - \mathbf{q}_\rho}{q_\rho^2 + k_v^2 - k^2} e^{i\mathbf{q}_\rho \cdot \boldsymbol{\rho}} \\ &= \frac{i e}{2\pi \epsilon_0 v} e^{ik_v x} \left[\underbrace{\frac{k_v}{\gamma^2} \int_0^{q_c} dq_\rho \frac{q_\rho J_0(q_\rho \rho)}{q_\rho^2 + k_v^2 - k^2}}_{\triangleq L_{q_c} \rightarrow \kappa_\rho K_0(\kappa_\rho \rho)/\gamma \text{ for } q_c \rightarrow \infty} \hat{\mathbf{x}} + i \underbrace{\int_0^{q_c} dq_\rho \frac{q_\rho^2 J_1(q_\rho \rho)}{q_\rho^2 + k_v^2 - k^2}}_{\triangleq T_{q_c} \rightarrow \kappa_\rho K_1(\kappa_\rho \rho) \text{ for } q_c \rightarrow \infty} \hat{\boldsymbol{\rho}} \right], \end{aligned} \quad (\text{S25})$$

reproducing Eq. (2) as $q_c \rightarrow \infty$ (we remind that $\kappa_\rho \triangleq k_v/\gamma$). Written in terms of the transverse and longitudinal parts introduced in the above, L_{q_c} and T_{q_c} , the regularized version of Eq. (3) reads

$$P_\tau(\omega) \leq \frac{e^2 \omega \xi_\tau}{16\pi^3 \epsilon_0 v^2} \int dV \frac{|\chi|^2}{\text{Im} \chi} (L_{q_c}^2 + T_{q_c}^2). \quad (\text{S26})$$

To demonstrate the limits’ finiteness, we require the small- ρ behavior of L_{q_c} and T_{q_c} at finite q_c .

Since q_c is large, much larger than κ_ρ , this is straightforward—particularly for T_{q_c} :

$$\begin{aligned} T_{q_c} &\triangleq \int_0^{q_c} dq_\rho \frac{q_\rho^2 J_1(q_\rho \rho)}{q_\rho^2 + \kappa_\rho^2} = \int_0^\infty dq_\rho \frac{q_\rho^2 J_1(q_\rho \rho)}{q_\rho^2 + \kappa_\rho^2} - \int_{q_c}^\infty dq_\rho \frac{q_\rho^2 J_1(q_\rho \rho)}{q_\rho^2 + \kappa_\rho^2} \\ &\simeq \kappa_\rho K_1(\kappa_\rho \rho) - \int_{q_c}^\infty dq_\rho J_1(q_\rho \rho) = \kappa_\rho K_1(\kappa_\rho \rho) - \frac{J_0(q_c \rho)}{\rho}. \end{aligned} \quad (\text{S27})$$

The small- ρ behavior then follows from the small-argument asymptotics of the Bessel functions [for $x \ll 1$, $K_1(x) = x^{-1} - \frac{1}{2}x(\frac{1}{2} - \gamma_{\text{EM}} - \ln \frac{1}{2}x) + \mathcal{O}(x^3 \ln x)$ and $x^{-1}J_0(x) = x^{-1} - \frac{1}{4}x + \mathcal{O}(x^3)$ with γ_{EM} denoting the Euler–Mascheroni constant]:

$$T_{q_c} \simeq \frac{1}{2}q_c^2 \rho + \frac{1}{2}\kappa_\rho^2(\gamma_{\text{EM}} - \frac{1}{2})\rho + \frac{1}{2}\kappa_\rho^2 \ln\left(\frac{1}{2}\kappa_\rho \rho\right)\rho, \quad \text{for } \rho \ll q_c^{-1} \ll \kappa_\rho^{-1}. \quad (\text{S28})$$

Thus, the regularized transverse component T_{q_c} vanishes as $\rho \rightarrow 0$ —for slightly larger ρ -values, however, T_{q_c} has a global maximum: $\max_{q_c \rho} T_{q_c} \approx T_{q_c}(q_c \rho \approx 2.76) \approx 0.42q_c$ (assuming $q_c \gg \kappa_\rho$).

The longitudinal contribution L_{q_c} does not find as neat a closed form expression as Eq. (S27), though it may still be expressed in terms of known functions:

$$\begin{aligned} L_{q_c} &\triangleq \frac{\kappa_\rho}{\gamma} \int_0^{q_c} dq_\rho \frac{q_\rho J_0(q_\rho \rho)}{q_\rho^2 + \kappa_\rho^2} \simeq \frac{\kappa_\rho}{\gamma} \left[\int_0^\infty dq_\rho \frac{q_\rho J_0(q_\rho \rho)}{q_\rho^2 + \kappa_\rho^2} - \int_{q_c}^\infty dq_\rho \frac{J_0(q_\rho \rho)}{q_\rho} \right] \\ &= \frac{\kappa_\rho}{\gamma} \left\{ K_0(\kappa_\rho \rho) + \ln \frac{1}{2}q_c \rho + \gamma_{\text{EM}} - \frac{1}{2}\left(\frac{1}{2}q_c \rho\right)^2 {}_2F_3 \left[\begin{matrix} 1, 1 \\ 2, 2, 2 \end{matrix} \middle| -\left(\frac{1}{2}q_c \rho\right)^2 \right] \right\}, \end{aligned} \quad (\text{S29})$$

where ${}_2F_3$ is a generalized hypergeometric function with the asymptotic behavior $= 1 - \mathcal{O}[(q_c \rho)^2]$. The small- ρ behavior again follows from the Bessel function asymptotics [$K_0(x) = -\ln \frac{1}{2}x - \gamma_{\text{EM}} + \mathcal{O}(x^2 \ln x)$], such that:

$$L_{q_c} \simeq \frac{\kappa_\rho}{\gamma} \ln \frac{q_c}{\kappa_\rho}, \quad \text{for } \rho \ll q_c^{-1} \ll \kappa_\rho^{-1}. \quad (\text{S30})$$

Thus, the longitudinal contribution L_{q_c} tends to a finite, nonzero value $\propto \ln q_c/\kappa_\rho$ as $\rho \rightarrow 0$; this is also the maximum of L_{q_c} .

Equations (S28) and (S30) demonstrate that the $\rho = 0$ singularity of the incident field is regularized for finite cut-off momenta q_c . This ensures that both direct calculations and limits similarly yield finite, regularized values, with bulk contributions dependent on the cut-off momentum.

7. EXPERIMENTAL METHODS AND DATA ANALYSIS

We are able to obtain the *absolute* intensity of Smith–Purcell radiation by implementing a calibration measurement using a broadband (visible and near infrared) calibrated source (AvaLight-HAL-CAL). The experimental setup for calibration is shown in Fig. S3. All the optics remain the

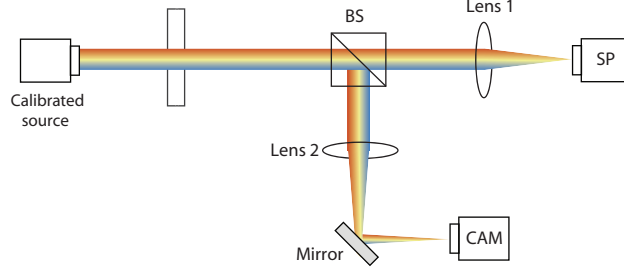


Figure S3. Experimental setup of the calibration measurement.

same as Fig. 3(a) except that we replace the SEM with the calibration source. The spectral intensity $S_0(\omega)$ of the calibrated source is already known from the manufacturer. Passing through all the optics, the radiation from the calibrated source enters the spectrometer and generates a signal count $C_0(\omega)$.

With $S_0(\omega)$ and $C_0(\omega)$, we are able to gauge Smith–Purcell radiation intensity $S(\omega)$ by reading the corresponding signal count $C(\omega)$. The relation is given by

$$\frac{S_0(\omega)}{C_0(\omega)} = \frac{S(\omega)}{C(\omega)}. \quad (\text{S31})$$

This relation is valid for two reasons. First, the generated photons into the sample substrate is negligibly small compared to the total radiation (see Fig. S4). Second, the optics and spectrometer configurations remain unchanged for Smith–Purcell radiation measurement and calibration measurement. This approach allows us to obtain the absolute radiation intensity of the collected Smith–Purcell radiation, without knowing the loss functions of each individual optical elements or the quantum efficiencies and EM gains of the spectrometer at each wavelength, since all these factors will cancel out if inserted into Eq. (S31).

To calculate the number of photons generated per electron, measurement of the current from the SEM is necessary. The currents are measured using a picoammeter connected to a built-in Faraday cup inside the SEM chamber. The measured currents are shown in Fig. S5(a).

For comparisons with the analytical limits, we also need to evaluate the number of unit cells N_{uc} of interaction and consider the beam diameters (spatial spread) of the electron beams. We estimate the electron beam diameter D with the equation [7]

$$D^2 = D_0^2 + D_d^2 + D_s^2 + D_c^2 = [C_0^2 + (0.6\lambda)^2]\alpha_p^{-2} + \frac{C_s^2\alpha_p^6}{4} + \left(C_c \frac{\Delta E}{E}\right)^2 \alpha_p^2. \quad (\text{S32})$$

Here D_0 is the aberration-free Gaussian probe diameter, D_d corresponds to aperture diffraction, D_s corresponds to spherical aberration, and D_c corresponds to chromatic aberration. Our SEM

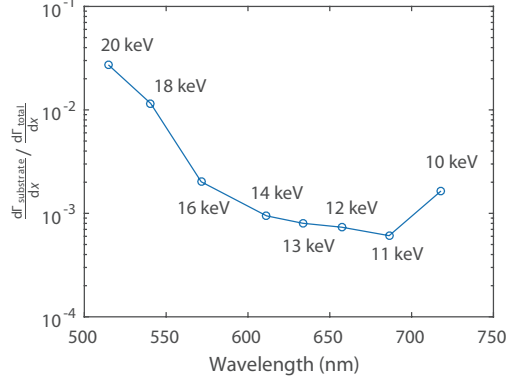


Figure S4. Fraction of the generated photons into the substrate for different accelerating energies at normal emission angle ($\lambda = a/\beta$) for the first-order Smith–Purcell radiation.

uses a tungsten thermionic cathode, for the energy regime (10–20 keV) we use, D_d and D_c are negligible [8]

$$D^2 \approx D_0^2 + D_s^2 = C_0^2 \alpha_p^{-2} + \frac{C_s^2 \alpha_p^6}{4}, \quad (\text{S33})$$

where

$$C_0 = \sqrt{4I/b\pi^2}, \quad (\text{S34})$$

b is the electron gun brightness, I is the probe current, α_p is the convergence semi-angle of the electron beam, and C_s is the spherical aberration coefficient. For the brightness b of the source, we choose 1×10^5 A/cm²/sr for the acceleration energy 20 keV (typical value for a tungsten source [7–9]) and scale it linearly [7–9] for other voltages. The focal length (working distance) of our SEM is 28 mm, which corresponds to a spherical aberration coefficient $C_s \approx 300$ mm [8, 9].

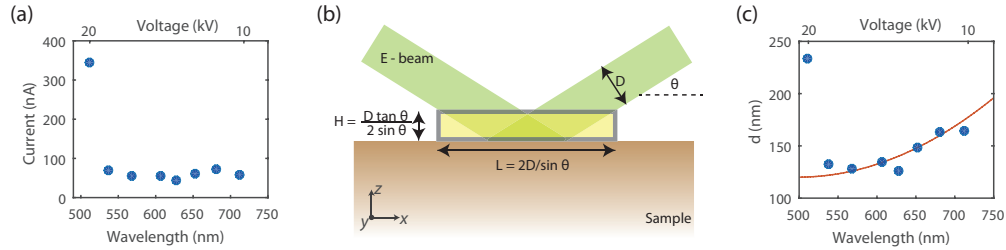


Figure S5. (a) Measured current of the experiment. (b) Schematic of the model to evaluate the interaction length of the electron beam with the structure. (c) Electron structure separations d obtained from the model (dots) and their polynomial fitting (curve; the 20 kV outlier data point dropped from fitting) for calculating theoretical upper limits.

For each measurement, we adjusted the SEM to achieve the smallest possible beam diameter. In theory, this corresponds to $D_{\min} = (4/3)^{3/8}(C_0^3 C_s)^{1/4}$ for the optimal convergence semi-angle $\alpha_{\text{opt}} = (4/3)^{1/8}(C_0/C_s)^{1/4}$ [derived from Eq. (S33)].

In our experiment, the electron beams grazingly impinges onto the sample at an nonzero angle of $\theta = 1.5^\circ$, which leads to a finite number of unit cells where electrons strongly interact with the structure such that the radiation contribution from other areas are negligible. The backscattering coefficient η of the SEM can be generally estimated as [7]

$$\eta = 1/(1 + \sin \theta)^p, \quad (\text{S35})$$

where $p = 9/\sqrt{Z}$ and Z is the atomic number. In our case, $\theta = 1.5^\circ$ and $Z = 79$ (Au), and thus $\eta \approx 0.974$, meaning that most electrons get elastically scattered and maintain their initial momenta, which correspond to the scenario shown in Fig. S5(b). The highlighted rectangle is treated as the region where electrons strongly interact with the structure. The number of unit cells is consequently determined via the length of the interaction region $N_{\text{uc}} = L/a = 2D/a \sin \theta$. After obtaining N_{uc} , the measured radiation spectral density $S(\omega)$ can be translated into emission probability per electron per frequency per unit propagation length

$$\frac{d\Gamma_{\text{expt}}(\omega)}{dx} = \frac{eS(\omega)}{\hbar\omega I N_{\text{uc}} a}, \quad (\text{S36})$$

which produces the measured emission probability shown in Fig. 3(d).

On the theory side, the upper limit in Fig. 3(d) is calculated for Smith–Purcell radiation at the surface-normal emission angle (i.e., $\beta = a/\lambda$). The limit is evaluated at the center of the interaction region with separation $d = H/2 = D \tan \theta/4 \sin \theta$ [see Fig. S5(c)] by generalizing Eq. (6). The generalization of Eq. (6), analogous to the expression of Eq. (4), is straightforward for the inhomogeneous Au-Si grating sample: move $|\chi|^2/\text{Im}\chi$ into the integrand, and account for different materials:

$$\Gamma_{\tau}(\omega) \leq \frac{\alpha \xi_{\tau} c}{2\pi\omega^2} \sum_{\text{mat}} \int_{V_{\text{mat}}} \frac{|\chi_{\text{mat}}|^2}{\text{Im}\chi_{\text{mat}}} \left[\kappa_{\rho}^4 K_0^2(\kappa_{\rho}\rho) + \kappa_{\rho}^2 k_v^2 K_1^2(\kappa_{\rho}\rho) \right] dV, \quad (\text{S37})$$

where V_{mat} and χ_{mat} are the occupied volume and susceptibilities of the materials ($\text{mat} \in \{\text{Si}, \text{Au}\}$).

8. NEAR-INFRARED SMITH–PURCELL RADIATION EXPERIMENT

We also conduct near-infrared experiment to further confirm out theory with the same experimental setup and a near-infrared spectrometer. A one-dimensional grating (Au-covered patterned-

Si, see Fig. S6 inset; LightSmyth Technologies) with a longer periodicity (≈ 272 nm) is used such that the Smith–Purcell radiation moves to near–infrared.

Adopting the same methods of data acquisition, calibration, and analysis [as those of our initial experiment in the visible (as described in Supplementary 7)], we are able to obtain the absolute emission probabilities for the near–infrared Smith–Purcell radiation. The new experimental results are shown in Fig. S6, where the envelope lineshape of the emission spectra again follows our theoretical prediction. The measured currents and the calculated electron structure separations are shown in Fig. S7.

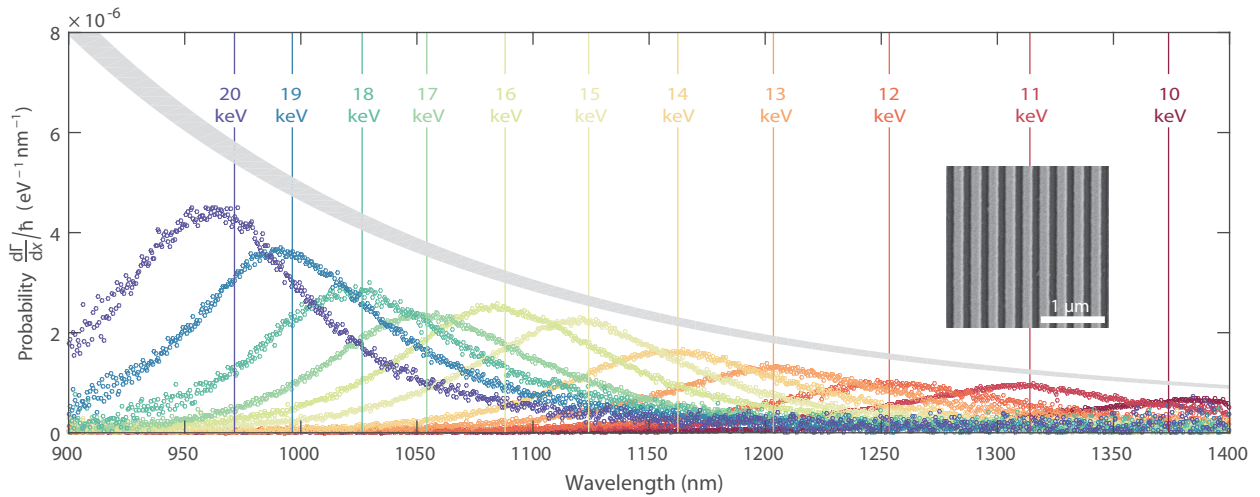


Figure S6. Smith–Purcell radiation observed in the near–infrared regime and the comparison with the upper limit theory.

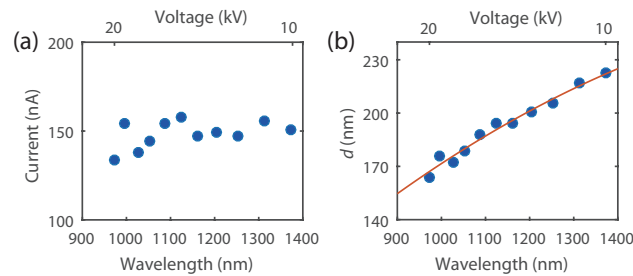


Figure S7. (a) Measured current of the near–infrared experiment. (b) Electron structure separations d obtained from the model (dots; see Supplementary 7) and their polynomial fitting (curve) for calculating theoretical upper limits.

In addition to the agreement between our theory and each of the experiment, the comparison between the visible and the infrared experiment gives rise to interesting observations that further

confirm our theory. Two key observations can be made from the comparison. First, the absolute emission probabilities increase by about two orders of magnitude from the visible to the near-infrared regime—consistent with the same order of increase in the material factor of Au [see Fig. 1(b)], which confirm the material factor dependence explicitly. Second, although the two experiments are both in the fast-electron-efficient regime, the measured emission probabilities feature a peak for the visible experiment, while exhibit monotonic decrease for smaller electron energies (except for a small increase between 17 keV to 16 keV) for the near-infrared experiment. Such a difference arises because the material response is much less dispersive in the near-infrared, which implicitly corroborates the functional impact-parameter dependence within our upper limit.

9. COMPLEMENTARY EVIDENCE FOR THE SLOW-ELECTRON-EFFICIENT PREDICTION

In the main text, we predict that slow electrons radiate more strongly than relativistic ones at subwavelength separation ($kd \ll 1$) with structures. We also provide numerical evidence for this prediction [Fig. 2(b-c)]. In this section, we discuss a complementary supporting evidence for our slow-electron-efficient prediction based on data extracted from a recent work [10] that reports an integrated Cherenkov radiator using hyperbolic metamaterials (Au/SiO₂ layered stack). The electron-structure separation is reduced by integrating the electron field emitter on the chip. Ref. [10] reports the output power P_{out} of the device as a function of anode-cathode currents I_{ac} and electron energies for fixed radiation wavelengths (centered at ≈ 780 nm; see Fig. 2 in Ref. [10]). These data allow us to extract the experimental emission probabilities $\frac{d\Gamma(\omega)}{dx} \propto P_{\text{out}}/I_{\text{ac}}$, since the reported shapes of the radiation spectra are similar for various electron energies (i.e., almost constant emission bandwidth for various electron energies).

The probabilities are therefore shown in Fig. S8, where data reported with electron energies are shown with extra red circles. Data points without electron energies reported in [10] are interpreted as linearly-interpolated electron energies. As we explicitly show in Fig. 2, the lineshape of emission probabilities versus electron velocity contains one-to-one correspondence with kd . Hence, the experimental lineshape can be fitted with the shape-independent upper limit [Eq. (5a)] to extract the electron-structure separation d (being the only free parameter to compare with the reported value):

$$\frac{\Gamma_{\text{rad}}(\omega)}{dx} \propto \frac{|\chi_{\text{eff}}|^2}{\text{Im}\chi_{\text{eff}}\beta^2} \frac{1}{\beta^2} \left[(\kappa_{\rho}d)K_0(\kappa_{\rho}d)K_1(\kappa_{\rho}d) \right], \quad (\text{S38})$$

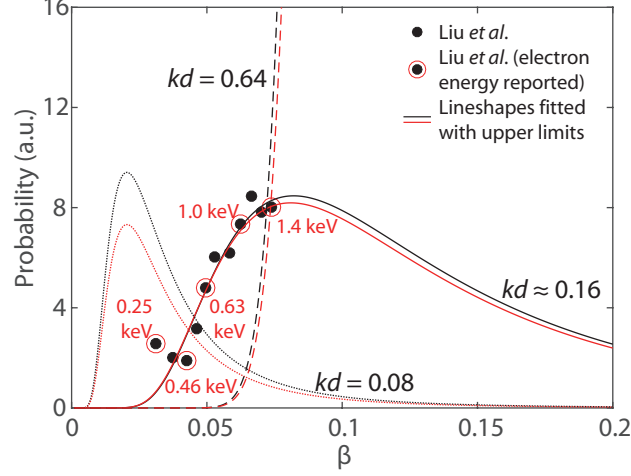


Figure S8. Extra external supporting evidence for the slow-electron-efficient prediction with small electron energies (0.25~1.4 keV), which complements our experiments using electrons with higher energies (10~20 keV). Extracted emission probabilities from [10] and the optimal lineshape fitting (solid lines with $kd \approx 0.16$) using the upper limit. The auxiliary suboptimal fittings (dashed and dotted curves) demonstrate the uniqueness of the extracted kd value. All red curves fit data points with electron energies reported, while all black curves fit all data points assuming linearly interpolated electron energies (see Fig. 2 in Ref.[10]).

where $\chi_{\text{eff}}(\chi_{\text{Au}}, \chi_{\text{SiO}_2}, \beta)$ is the effective susceptibility of the metamaterial, a function of the composite material permittivities and the longitudinal wavevector (i.e., the electron velocity), is explicitly determined from the standard effective medium theory (see Supplementary Information of Ref. [10] S1–S3 sections). We obtain two primary fitting results in Fig. S8, where $\hat{d}_1 = 20.0 \pm 2.3$ nm for the solid black curve (fits all data) and $\hat{d}_2 = 19.8 \pm 6.7$ nm for the solid red curve (only fits the data with electron energies reported). The estimated $kd \approx 0.16$ corresponds to an optimal nonrelativistic electron velocity $\beta_{\text{opt}} \approx 0.08$ (see Fig. S8). We emphasize that although the only available experimental data are below the predicted β_{opt} , they are sufficient for us to unambiguously extract the kd value for the experiment. The uniqueness of the kd value is supported by the two auxiliary suboptimal fittings (dashed and dotted curves) with either reduced or increased kd values.

For comparison, the reported separation from the field emitter to the structure is 40 nm. Since the electron beam in the reported device is still not theoretically ideal (not a delta function in space; instead, with nonzero beam diameters), we consider the estimates \hat{d}_1 and \hat{d}_2 , from our upper limit theory, as good agreement with the realistic structural parameter. Hence, such an agreement serves

as complimentary support for our prediction about the slow-electron-efficient regime.

10. UPPER LIMIT IN TWO DIMENSIONS

The limits can be derived in both the three-dimensional or the two-dimensional case. For completeness, here we also derive the limit in the two-dimensional case, which correspond to sheet electron beams that are assumed in Fig. 4(f).

We consider an electron sheet beam in the (x, z) plane with charge density being one electron per nanometer, i.e., $q = 1.6 \times 10^{-19}$ C/nm [consistent with our unit for probability in two dimensions $\frac{d^2\Gamma}{dx dy}/\hbar$ ($\text{eV}^{-1}\text{nm}^{-2}$)]. Precisely, the probability is invariant of the choice of the transverse (y) length scale, as long as the length scale is in the same unit for both the source current density and the probability. Here the length scale is chosen as nanometer for both of the quantities.

The source current density in the time domain can be written as $\mathbf{J}(\mathbf{r}, t) = qv\delta(z - z_0)\delta(x - vt)\hat{\mathbf{x}}$. In the frequency domain, the current density is given by

$$\mathbf{J}(\mathbf{r}, \omega) = q\delta(z - z_0)e^{ik_v x}\hat{\mathbf{x}}, \quad (\text{S39})$$

The induced fields are

$$\mathbf{H}(\mathbf{r}, \omega) = -\frac{q}{2}e^{ik_v x - \kappa_\rho(z - z_0)}\hat{\mathbf{y}} \quad (\text{S40a})$$

$$\mathbf{E}(\mathbf{r}, \omega) = \frac{q}{2\omega\epsilon_0}(k_v\hat{\mathbf{z}} - i\kappa_\rho\hat{\mathbf{x}})e^{ik_v x - \kappa_\rho(z - z_0)} \quad (\text{S40b})$$

for $z > z_0$ and

$$\mathbf{H}(\mathbf{r}, \omega) = \frac{q}{2}e^{ik_v x + \kappa_\rho(z - z_0)}\hat{\mathbf{y}} \quad (\text{S41a})$$

$$\mathbf{E}(\mathbf{r}, \omega) = -\frac{q}{2\omega\epsilon_0}(k_v\hat{\mathbf{z}} + i\kappa_\rho\hat{\mathbf{x}})e^{ik_v x + \kappa_\rho(z - z_0)} \quad (\text{S41b})$$

for $z < z_0$, where ϵ_0 is the vacuum permittivity, and κ_ρ also defined as $\kappa_\rho = \sqrt{k_v^2 - k^2}$, same as the main text. where $k = \omega/c$ is the light wavevector.

Insert Eq. (S41b) into Eq. (4), we obtain the limit in two dimensions

$$\frac{d\Gamma_\tau(\omega)}{dy} \leq \frac{|\chi|^2}{\text{Im}\chi} \frac{q^2 \xi_\tau (k_v^2 + \kappa_\rho^2)}{32\hbar\epsilon_0\omega^2} \int_S e^{-2\kappa_\rho|z - z_0|} dS, \quad (\text{S42})$$

where S is the area defined by the profile of the structure.

As in the main text, we also consider a concrete example: Smith–Purcell radiation from a rectangular grating with filling factor Λ . Applied the rectangular profile to Eq. (S42), the radiated photon per frequency per electron per unit area is bounded by

$$\frac{d^2\Gamma_\tau(\omega)}{dx dy} \leq \frac{|\chi|^2}{\text{Im}\chi} \frac{\Lambda q^2 \xi_\tau(k_v^2 + \kappa_\rho^2)}{64\hbar\epsilon_0\kappa_\rho\omega^2} e^{-2\kappa_\rho d}, \quad (\text{S43})$$

where d is the distance between the electron and the grating.

11. FREE ELECTRON RADIATION NEAR A BOUND STATE IN THE CONTINUUM

In photonic systems, modes below the light cone are guided modes, while modes above the light cone are typically resonances with finite lifetime. In contrast to guided modes or resonances, a bound state in the continuum is a perfectly confined modes with infinite lifetime embedded in the radiation continuum (above light cone) [11].

These properties can be used to distinguish whether an optical resonance is a BIC or not. The mode profile in Fig. 4(c) corresponds to a BIC because 1) it is obviously within the continuum [see Fig. 4(a)]; 2) it possesses infinite lifetime without external radiation (no outgoing oscillatory radiation in its eigenmode profile), as shown in Fig. S9(a).

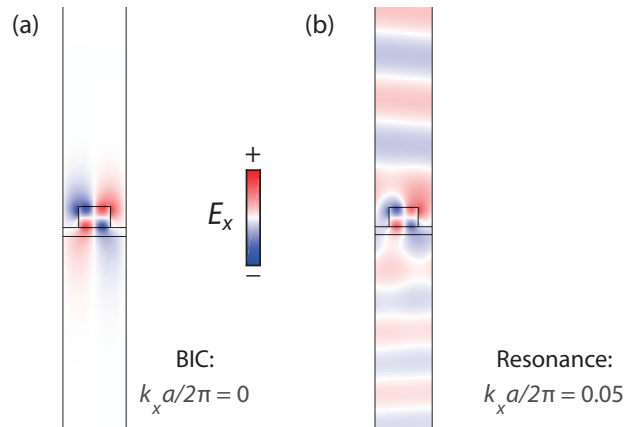


Figure S9. Difference of a BIC and a resonance on the TE_1 band of Fig. 4(a). (a) The mode profile of a BIC decays exponentially, giving rise to infinite lifetime; (b) The mode profile of a resonance contains oscillatory radiation into the far field, leading to finite lifetime.

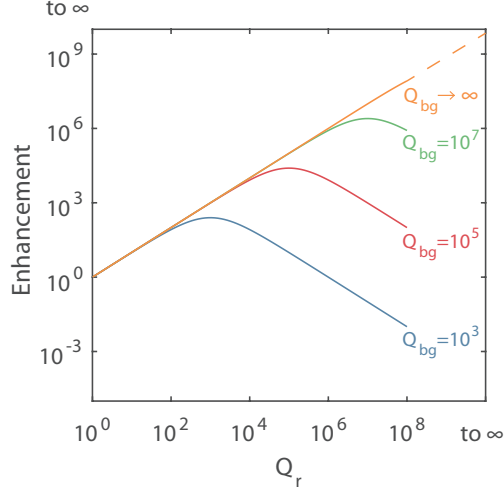


Figure S10. Smith–Purcell radiation enhancement as a function of resonant quality factors under different background quality factors.

Next we explain the Smith-Purcell radiation enhancement near a BIC. We write down the temporal coupled mode theory [12] for the coupling process

$$\frac{da}{dt} = -i\omega_0 a - a \left(\frac{1}{\tau_{\text{bg}}} + \frac{1}{\tau_r} \right) + \sqrt{\frac{2}{\tau_r}} s_+, \quad (\text{S44})$$

where a is the mode amplitude inside the resonances, $1/\tau_{\text{bg}}$ is the background coupling rate (such as material absorption and scattering loss due to fabrication impefections), $1/\tau_r$ is the resonant coupling rate (for BIC, $\tau_r = \infty$), s_+ is the wave amplitude carried by the electron towards the resonances. Solving Eq. (S44) for a we have

$$\left| \frac{a}{s_+} \right|^2 = \frac{2/\tau_r}{(\omega - \omega_0)^2 + \left(\frac{1}{\tau_{\text{bg}}} + \frac{1}{\tau_r} \right)^2} \quad (\text{S45})$$

Assuming on-resonance condition ($\omega = \omega_0$, electron line and photonic bands intersects), to maximize the resonance amplitude for a given fixed s_+ , we have

$$\left| \frac{a}{s_+} \right|^2 = \frac{2/\tau_r}{\left(\frac{1}{\tau_{\text{bg}}} + \frac{1}{\tau_r} \right)^2} \propto \frac{Q_{\text{tot}}^2}{Q_r}. \quad (\text{S46})$$

where $Q = \omega\tau/2$ for all channels and $1/Q_{\text{tot}} = 1/Q_r + 1/Q_{\text{bg}}$. It is thus evident from Eq. (S46) that the maximal resonance enhancement is achieved when $Q_{\text{bg}} = Q_r$, (i.e., $\tau_{\text{bg}} = \tau_r$) which is the “Q-matching condition” we refer to in the manuscript.

As a result, the achievable radiation enhancement depends on the background radiation rate (see Fig. S10). In our example shown in Fig. 4(f) with material absorption taken into account, the maximal enhancement occurs at small offsets from the BIC with a $Q_r \approx 10^3 \sim 10^5$.

-
- [1] A. Welters, Y. Avniel, and S. G. Johnson, *Phys. Rev. A* **90**, 023847 (2014).
 - [2] F. G. De Abajo, *Rev. Mod. Phys.* **82**, 209 (2010).
 - [3] J. D. Jackson, *Classical electrodynamics* (John Wiley & Sons, 2007).
 - [4] M. Abramowitz and I. A. Stegun, *Handbook of mathematical functions: with formulas, graphs, and mathematical tables*, Vol. 55 (Courier Corporation, 1964).
 - [5] J. Kong, *Electromagnetic Waves Theory* (EMW Publishing, Cambridge, MA, 2005).
 - [6] C. S. Meijer, *Proc. Nederl. Akad. Wetensch.* **49**, 344 (1946).
 - [7] J. Goldstein, D. E. Newbury, D. C. Joy, C. E. Lyman, P. Echlin, E. Lifshin, L. Sawyer, and J. Michael, *Scanning Electron Microscopy and X-ray Microanalysis* (Springer Science & Business Media, 2012).
 - [8] L. Reimer, *Scanning electron microscopy: physics of image formation and microanalysis*, Vol. 45 (Springer-Verlag, 1998).
 - [9] A. Khursheed, *Scanning electron microscope optics and spectrometers* (World scientific, 2011).
 - [10] F. Liu, L. Xiao, Y. Ye, M. Wang, K. Cui, X. Feng, W. Zhang, and Y. Huang, *Nat. Photon.* **11**, 289 (2017).
 - [11] C. W. Hsu, B. Zhen, A. D. Stone, J. D. Joannopoulos, and M. Soljačić, *Nat. Rev. Mater.* **1**, 16048 (2016).
 - [12] J. D. Joannopoulos, S. G. Johnson, J. N. Winn, and R. D. Meade, *Photonic crystals: molding the flow of light* (Princeton university press, 2011).